POLITECNICO DI TORINO

Master's Degree in Aerospace Engineering

Master's Degree Thesis

Development and testing of a small scale hybrid rocket motor with a Novel Grain Geometry

Relatori

Prof. Giuseppe Dario PASTRONE

Dr. Patrick LEMIEUX

Dr. Filippo MASSENI

Dr. Andrea FERRERO

Candidato

Jacopo BONOTTO

December 2024

Abstract

In recent years, Hybrid Rocket Propulsion has received significant attention as a candidate for space propulsion due to its safety, ability to throttle, ability to restart compared to solid rockets and low cost, simplicity and compactness compared to liquid propulsion. However, this technology also presents issues that have hampered its large scale adoption. One of the most important ones is the low and uneven regression rate of the solid fuel grain. The post-burn analyses of most fuel grains show a non-uniform regression rate along the grain length, with an increased consumption of the solid fuel at the upstream end of the motor. Various types of solutions have been studied to solve this issue, such as swirl oxidizer injection, mechanical devices embedded in the solid fuel, metallic additives, and fuel grain geometries.

This thesis aims to build on the work previously carried out at the California Polytechnic State University, San Luis Obispo (USA), investigating the combined effects of a helical solid grain geometry (in order to enhance the regression rate of the fuel) with angular oxidizer injection, the goal being to induce swirl and improve the homogeneity of the burn axially along the grain, thus resulting in a more uniform regression rate along the chamber length.

The first part of this project focuses on the work done to bring Cal Poly's Hybrid Rocket Test Stand back to operational status. In the second part, we propose a new fuel grain geometry composed of a first cylindrical section followed by a second section, presenting helical guide vanes. The purpose of this geometry is to bring forward the swirl to the nozzle-end of the chamber, in order to obtain a more uniform regression rate between the beginning and the end of the chamber.

The objectives to be measured are the greater uniformity of the regression rate along the grain; furthermore, we intend to measure the improvement in the average regression rate compared to a traditional architecture (measured as a percentage increase).

Acknowledgements

I would like to thank my supervisors, Prof. Pastrone and Dr. Lemieux, for their guidance during this project. Thank you for allowing me to live this important educational experience, which made me grow as a person and as an engineer. Thank you to the technicians at Cal Poly, Graham and Cody, for your helpful support during these six months.

Thank you mom and dad for raising me to be who I am today and for always showing your unwavering support in everything that I set out to do. I will always be grateful for having you in my life. To my sister, thank you for inspiring me to always do better.

To my friends in Verona, thank you for always having time for a laugh and to spend even a little bit of time together. You have no idea how much I appreciate you.
To my friends in Turin, you have been the best companions I could ask for on this adventure and I treasure our friendship as some of the best I have. Thank you for putting up with my antics and always making me laugh.
To Aidan and Jake, you really are two wonderful friends. I'm glad I got to meet you during my time in the US and I can't wait to meet you again sooner or later.

Table of Contents

List of Tables

List of Figures

Acronyms and Nomenclature

a: Marxman Law Ballistic Coefficient

A_b: Burning Area

A_p: Port Area

B: Blowing Parameter

β: First Injector Angle

C_{f_0}: Skin Friction Coefficient without Blowing

C_f: Skin Friction Coefficient

c_v: Constant Volume Specific Heat

D: Diameter

e: Groove Depth

G: Total Mass Flux

G_o: Oxidizer Mass Flux

G_θ: Axial Flux of Swirl Momentum

G_x: Axial Flux of Axial Momentum

h: Enthalpy

h_v: Effective Heat of Gasification

HRE: Hybrid Rocket Engine

HRM: Hybrid Rocket Motor

LRE: Liquid Rocket Engine

SRM: Solid Rocket Motor

ID: Internal Diameter

γ: Second Injector Angle

m: Marxman Law Ballistic Coefficient

$\dot{m}$: Total Mass Flux

$\dot{m}_f$: Fuel Mass Flux

$\dot{m}_{ox}$: Oxidizer Mass Flux

μ: Viscosity

n: Marxman Law Ballistic Coefficient

OD: Outer Diameter

p: pressure

P: Thread Pitch

$\dot{Q}_c$: Convective Heat Flow

$\dot{Q}_r$: Radiative Heat Flow

$\dot{Q}_w$: Wall Heat Flow

r: radius

$\dot{r}$: Regression Rate

Re: Reynolds Number

ρ: Density

S: Swirl Number

St: Stanton Number

T: Temperature

τ: Shear Stress

u: Axial Direction Speed

w: Tangential Direction Speed

W: Groove Width

x: Axial Distance From Grain Entry

Chapter 1

Introduction

This project aims at studying the effects of helical grooves on the regression rate in hybrid rocket motors (HRM) with swirl injection schemes.
Before diving into the topics of the thesis it's important to introduce the concepts of hybrid rockets and the main differences with conventional chemical rockets.

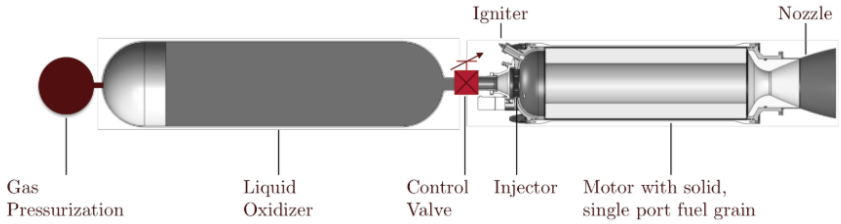

Figure 1.1: Scheme of a typical HRE

1.1 Hybrid Rocket Motors

HRMs are a rocket propulsion bipropellant option in which one component is stored as a liquid (usually the oxidizer) and the other as a solid (usually the fuel) [1]. They can be viewed as a trade-off between liquid and solid rocket propulsion.
In recent years HRMs have received significant attention as candidates for space propulsion due to their advantages compared to liquid (LRE) and solid propulsion (SRM); these advantages are:

- **Safety**: this is often one of the most desirable characteristics of hybrid propulsion. Fuel and oxidizer are stored separately and usually not in critical conditions, lowering the hazard of explosions almost to zero. HRMs also

have high ruggedness, so they can withstand the effects of bullet impacts and inadvertent droppings.

- **Ability to throttle**: an advantage over Solid Rocket Motors is that HRMs offer the possibility to be stopped, restarted and throttled.
- **Simplicity**: compared to liquids, which may translate to lower system cost and higher reliability (in HRMs only half of the feeding system is necessary, for the oxidizer, unlike in liquid bipropellant engines).
- **Environmental friendliness**: most propellant combinations for hybrid rockets generate clean exhaust gasses.
- **Low cost**: operational costs for this type of rockets is greatly reduced by their safety features. Further savings are related by the innate insensitivity to crack of the solid grain.

Classical HRMs also present a number of disadvantages [2], such as:

- **Performance**: hybrid rockets have a lower specific impulse compared to cryogenic bipropellant LREs and have lower density specific impulse compared to solid rocket motors.
- **Low fuel regression rate**: conventional fuels such as HTPB and PMMA typically have regression rates that are an order of magnitude lower than solid propellants; this translates to the need of having larger internal surfaces to produce the required thrust. This limit is usually set by the physical phenomenon of heat transfer from the diffusion flame to the grain surface.
- **Mixture ratio shifting**: during the combustion of the grain, the port area A_p increases leading to a regression rate reduction. At the same time the burning area A_b increases as well. These two phenomena are not balanced even if the oxidizer mass-flow is constant; this leads to the shifting of the mixture ratio and performance is worsened.
- **Mixing inefficiencies**: HRMs have lower combustion efficiency than liquid and solid propulsion.
- **Slow response to throttling**: due to the thermal lag in the solid grain, ignition and throttle are slower than LREs. HRMs often require a gentle introduction of the oxidizer in order not to extinguish the flame generated by the ignition gasses.

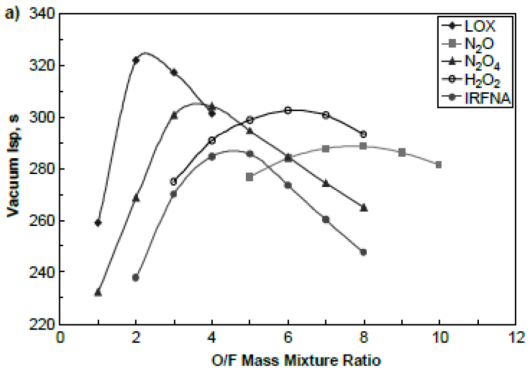

Figure 1.2: Specific Impulse over O/F ratio for different propellant combinations

1.2 Hybrid Rockets History and Development

The history of HRMs goes back to the 1930s, when the first known hybrid rocket motor, using LOX and gelled gasoline was tested in the Soviet Union [3]. Shortly after, German tests followed, using N2O and LOX as oxidizer and coal and graphite as fuel respectively. Even though little literature can be found regarding the first stages of HRM studies, it is almost certain that they were driven by the military needs for rocket applications.
The time frame between 1960 and 1980 is considered the "Enlightment Era" for HRM, as extensive experimental and modelling advances were made [3]. A key output of this era would be Marxman's comprehensive theoretical treatment of hybrid rocket fuel combustion.
In more recent years, an important role was played by SpaceShipOne, a smaller commercial version of the Space Shuttle developed by Scaled Composite with a hybrid propulsion system (made by SpaceDev), which, in a well-publicized accomplishment, won the Ansari X-Prize when it reached space in 2004 with two suborbital manned flights [1].

Figure 1.3: StarShipOne during glide down. The propellant for this configuration is HTPB-N2O

Modern (post-2005) space transportation developments using hybrid rocket motors are being conducted worldwide and the majority have been initiated after 2015 [3]. Advanced laboratory-scale R&D with no openly disclosed information on particular vehicles takes place in several countries, including Italy.
In some cases companies flew sub-scale demonstrators not allowing to reach altitudes beyond those available to planes, but providing key data for further developments. The dynamic growth of the number of student hybrid rocket propulsion initiatives is evident in recent years. This is due to inter alia ease of handing and operational safety, but also limited restrictions regarding propellant procurement and transport.

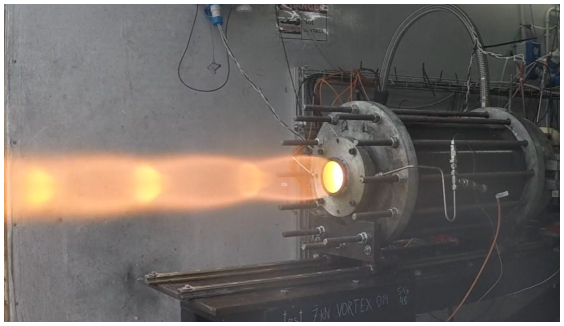

Figure 1.4: TEIDE hybrid propellant from T4i, an italian company

1.3 Project Motivation

Even though HRMs have received significant attention in recent years, this technology presents challenges that need to be addressed in order to reach a large scale adoption. One of these challenges is the low and uneven regression rate of the solid grain; for this, a number of solutions have been studied, such as swirl injection and different grain shapes.
This project aims at developing a novel helical grain geometry that, paired with a swirl injection scheme, is predicted to improve the homogeneity of the regression rate of the hybrid rocket motor at Cal Poly's Engine Lab.

1.4 Project Goals

Modelling and testing a hybrid rocket is a task that can be taken to varying levels of complexity, the precision level and diversity of the tests conducted was chosen to make the most out of the time available. Naturally, the main goal is to obtain an enhancement in the average regression rate and better, homogeneous local

regression rate along the grain length.
The objectives of the thesis can be categorized as follows:

- **Test Stand Refurbishment**: the first goal of the project is to be able to bring the test bed back to an operational state. This means re-calibrating the instrumentation and correctly set up the data acquisition system to work with a new, more modern, software.
- **Fuel Grain Development and Testing**: once the system is set up, the geometric characteristics of the HRM solid grain will be designed and the configuration tested with the goal to produce an increase in the regression rate, both on average and locally.

Chapter 2

Hybrid Motor Internal Ballistics

Ignition of hybrid fuel grains is usually provided by a source of heat that initiates the gasification of the grain at the head-end of the motor. In large scale applications, ignition is typically accomplished by injection of a hypergolic fluid combination into the combustion chamber [1]. For small scale applications (such as rockets used in laboratory environments), the motor can be electrically ignited by passing current through a resistor, or by using a separate propane or hydrogen ignition system.

2.1 Physics of the Combustion Process

The theory for classical hybrid rocket fuels combustion is summarized in this section. The analysis assumes the following: steady state combustion, the flame occupies an infinitely thin layer and the combustion doesn't significantly alter the velocity profile in the in the boundary layer [4, 5, 6]. The schematic of the model is shown in Fig. 2.1.

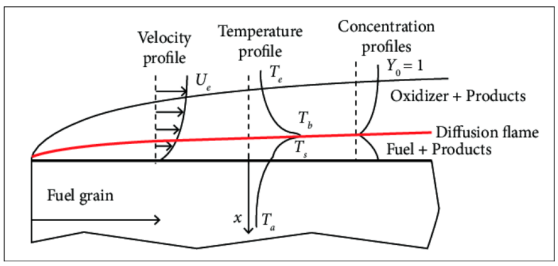

Figure 2.1: Schematic of diffusion-limited combustion processes in a turbulent boundary layer with blowing for a classical fuel

A boundary layer develops over the solid grain when the oxidizer is injected into the chamber. After ignition, a diffusion flame is formed near the wall, at about 10-20% of the boundary layer thickness (as showed by the red line in Fig. 2.1).

The flame establishes itself at a location within the boundary layer determined solely by the stoichiometry under which combustion can occur [1], and it's sustained by the oxidizer flowing into the combustion chamber and the thermal decomposition of the grain (pyrolysis) that makes the fuel evaporate from the surface. The main factor that influences the flame thickness is the rate at which oxidation reactions occur.

The velocity of consumption of the fuel is described by the regression rate $\dot{r}$, defined as the rate at which the solid grain is converted into gas and has the dimensions of a velocity.
Factors beyond pressure and gas temperature affecting the development of the fuel grain boundary layer, and hence fuel regression characteristics, include grain composition, combustion port oxidizer mass flow rate, and combustion port length and cross-sectional area [1].

2.2 Marxman Model for Regression Rate

The most influential regression rate model was developed by Marxman et al. in the 1960s. In this theory it's assumed that the velocity profile of the oxidizer is uniform at the grain entrance and that the wall boundary layer is developing along the grain length; furthermore, the boundary layers on the opposite sides of the wall don't merge.

The fundamental equation for this model is the conservation of energy, applied at the grain surface, that gives the equivalence between the heat transferred to the wall and the energy required for the gasification of the fuel (Eq. 2.1).

$$\frac{\dot{Q}_w}{h_v} = \rho_f \dot{r} = (\rho v)_w \tag{2.1}$$

Where $\dot{Q}_w$, ρ_f, h_v are respectively the wall heat flow, the solid fuel density and the heat of gasification. The total heat transfer to the fuel surface $\dot{Q}_w$ can be expressed as the addition of the convective and radiative heat transfer:

$$\ddot{Q}_w = (\dot{Q}_c)_w + (\dot{Q}_r)_w \tag{2.2}$$

The authors assumed that $Pr = 1$, so that the Reynolds' Analogy is valid within the turbulent boundary layer, but not at the location of the flame. The analogy

can then be written as an equivalence between the convective wall heat flux $(\dot{Q}_c)_w$ and the wall shear stress τ_w

$$\frac{(\dot{Q}_c)_w}{\Delta h_t} = \frac{\tau_w}{u_b} \tag{2.3}$$

Where Δh_t is the difference in gas enthalpy between the flame zone and the region adjacent to the wall and u_b is the axial velocity of the combustion products in the flame zone.
The equation can be re-written in a dimensionless form introducing the Reynolds and Stanton numbers and using the expression for the skin friction for a turbulent boundary layer without blowing.

$$St = \frac{(\dot{Q}_c)_w}{\Delta h_T \rho_b u_b} \tag{2.4}$$

$$Re = \frac{\rho_e u_e x}{\mu_e} \tag{2.5}$$

$$C_{f_0} = 0.06 Re_x^{-0.2} \tag{2.6}$$

By using Eq. 2.6 the authors are assuming that the presence of blowing does not alter the nature of the flow.
It's now possible to substitute in Eq. 2.1; by neglecting the heat transfer by radiation ($\dot{Q}_w = (\dot{Q}_c)_w$), Marxman obtained:

$$\rho_f \dot{r} = 0.03 \rho_e u_e Re_x^{-0.2} \frac{C_f}{C_{f_0}} \frac{u_e}{u_b} \frac{\Delta h_T}{h_v} \tag{2.7}$$

Where $\frac{C_f}{C_{f_0}}$ is a correction factor introduced to take into account the presence of blowing. To account for the differences between the combusting case with blowing and the non-combusting case, the blowing parameter B is defined.

$$B = \frac{2(\rho v)_w}{\rho_e u_e C_f} = \frac{\Delta h_T}{h_v} \frac{u_e}{u_b} \tag{2.8}$$

It is a thermochemical quantity, that depends on the position of the flame in the boundary layer and on the propellants used.
In [6], Marxman derived an approximation (Eq. 2.9) for the correction ratio $\frac{C_f}{C_{f0}}$ as a function of the blowing parameter when it is in the range $5 \leq B \leq 100$.

$$\frac{C_f}{C_{f0}} \approx 1.2 B^{-0.77} \tag{2.9}$$

This allows to write the regression rate as following, thanks to the use of the total max flux $G = \frac{\dot{m}}{A_p}$

$$\rho_f \dot{r} = 0.03 G \left(\frac{Gx}{\mu_e} \right)^{-0.2} B^{0.23} \tag{2.10}$$

If the radiative heat transfer is neglected and a constant A is defined for a given propellant combination, then the equation can be rewritten as Eq. 2.11

$$\dot{r} = AG^{0.8}x^{-0.2} \tag{2.11}$$

A more common form is shown below, where a, m and n are empirically determined constants for a given fuel and oxidizer combination.

$$\dot{r} = aG^{n}x^{-m} \tag{2.12}$$

This equation is very important, as it states that the burn rate of an hybrid rocket's fuel is a function of only the mass flux in the combustion chamber and the axial location along the length of the grain. Unlike SRM, it is not dependent on the chamber pressure under typical conditions.

It's important to notice that the total mass flux G includes both the oxidizer and the fuel mass fluxes ($\dot{m}_{ox}$ and $\dot{m}_{fuel}$ respectively). The oxidizer mass flow rate can be assumed constant along the chamber length, but the fuel mass flow rate increases with the axial distance because of the vaporization of the fuel.

Fig. 2.2 shows there are three distinct regimes as a function of increasing mass–flow–velocity in the free stream [1].

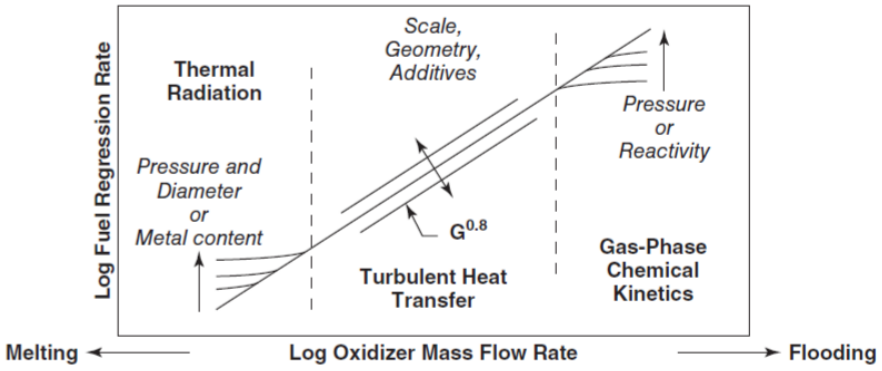

Figure 2.2: Hybrid regimes of regression rate dependencies [1]

With low mass flux, radiative heat transfer manifests in the form of pressure and diameter effects on the optical transmissivity of the propellant gas. A lower limit of the mass flux exists, at which the regression rate is so small that the fuel starts "cooking" (internal layers of the grain melt); if this happens, chuffing instability may be produced [2] and the grain might result "charred" visually.
For the medium G range, the phenomenon is diffusion dominated and the regression

rate is a function of the mass flux.
At higher G values, effects from gas-phase kinetics on chemical reactions are apparent and a different type of pressure dependence appears. An upper limit exists, called flooding limit; when close to this limit, the mass flux may be high enough that the flame is extinguished due to small Damköhler numbers and/or oxidizer rich conditions [2].

2.2.1 Injection Effects on Marxman Theory

Among the hypotheses that lead to the writing of Eq. 2.12 are that the velocity profile is uniform at the grain entrance and the presence of a developing turbulent layer. This makes the model not suitable to describe the regression rate in the entrance zone of the grain, as this zone is dominated by the injector effects.

Various studies analyzed the effects of different type of injectors during the years. In [7], the authors investigate the effects of axial and radial injection in the system. Two series of experimental tests are performed, the first with a single axial injector, and the second with a radial injection system.
Fig. 2.3 shows the differences in the regression rates along the grain length for the two types of injection. It can be seen that the diameter profiles for the radial injection are quite uniform and in good agreement with the theory. This is not the case for the axial injection scheme.

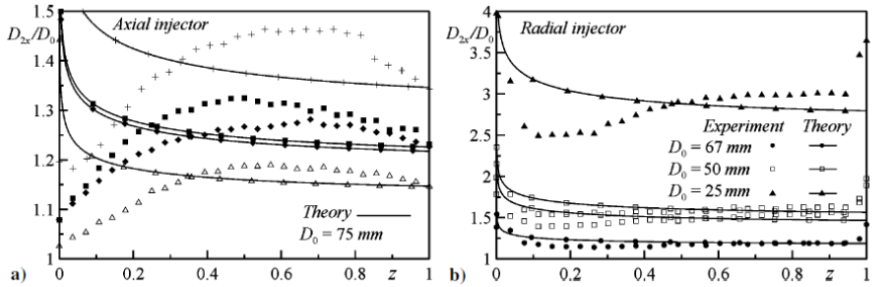

Figure 2.3: Post firing diameters with axial (a) and radial (b) injection

The study suggests that the difference is due to the axial injection producing a recirculation zone between the gaseous oxidizer jet boundary and the grain surface, responsible for the enhancement of the convective heat flux to the wall. This means that the maximum regression rate is in proximity of the jet impingement point.

A very interesting aspect of the setup is that it produces stable combustion with considerably small pressure oscillations.

Chapter 3

Swirl Flows

3.1 Swirl Flow Characterization

In combustion systems, swirl is often used as an aid to stabilization of the flame and to reach cleaner and efficient combustion.
Swirling flows are created when a spiraling motion is imparted to the flow by the use of swirl generators (such as: vanes, axial-plus-tangential entry generators, direct tangential entry) that provide a swirl velocity component.

The degree of swirl is usually characterized by the swirl number S [8], a non-dimensional number defined by the ratio of axial flux of swirl momentum over axial flux of axial momentum times the equivalent radius:

$$S = \frac{G_\theta}{G_x d/2} \tag{3.1}$$

When S is calculated, turbulent stress terms can be omitted. In this formulation G_θ and G_x (axial flux of swirl momentum and axial momentum respectively) are constants and therefore invariants of the jet flow. However, this quantities are often difficult to measure.
If solid body rotation plug flow at the nozzle is assumed, the following deduction can be made for the axial velocity u and the swirl velocity w:

$$u = u_{m0}; \qquad w = w_{m0}\frac{r}{d/2} \tag{3.2}$$

This is basically assuming that axial velocity is a constant flat profile and that swirl velocity goes from 0 (at $r = 0$) to w_{m0} (at $r = d/2$) [8]. Introducing $G = w_{m0}/u_{m0}$ the swirl number can be written as follows.

$$S = \frac{G/2}{1 - G/2} \tag{3.3}$$

It's very useful to be able to relate the angle of a swirl generator with the swirl number it produces; in the case of a hubless swirl generator, swirl vane angle and swirl number are related approximately by Eq 3.4.

$$S = \frac{2}{3}\tan(\phi) \tag{3.4}$$

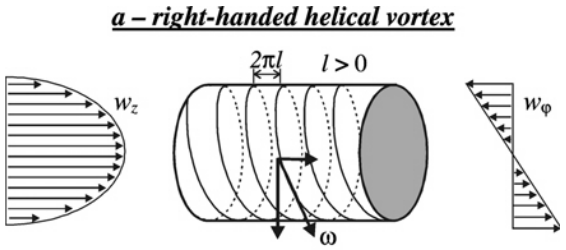

Figure 3.1: Visual representation of swirl flow and velocity fields

3.1.1 Basic Effects of Swirl

The effects of swirling on the following flow field increase as the degree of swirl increases. It's possible to define different type of behaviour, based on the swirl intensity:

- The effect of low degree of swirl ($S <\simeq 0.4$) is to increase the width of the jet (whether free or confined): jet growth, entrainment and decay are enhanced progressively as the degree of swirl is increased.
  - For very weak swirl ($S <\simeq 0.2$) pressure gradients can be omitted from the analyses. Swirl velocities decay rapidly with downstream distance.
  - At low degrees of swirl, the adverse pressure gradient is not enough to cause axial recirculation.
- The effect of strong swirl ($S >\simeq 0.6$) is to increase previously mentioned effects, plus, strong radial and axial pressure gradients are set up, resulting in axial recirculation in the form of a central toroidal recirculation zone (CTRZ). For combustion applications, one of the most useful phenomena is precisely the CTRZ generated for supercritical swirl numbers ($S \simeq 0.6$).

The recirculation zone aids the flame stabilization, as it provides a hot flow of recirculated combustion products and a region with reduced velocity in which flame speed and flow velocity can be matched. It also enhances the mixing.

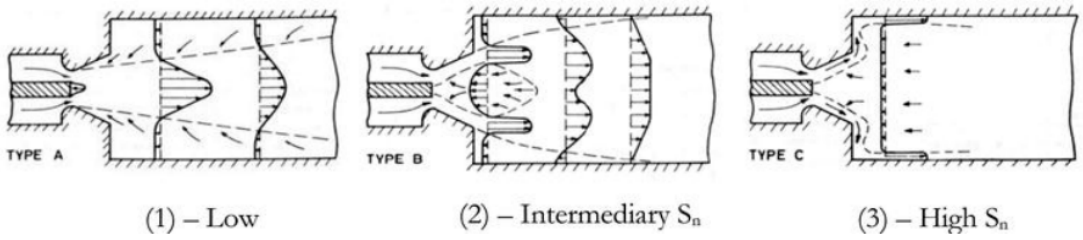

Figure 3.2: Swirl effects on flames

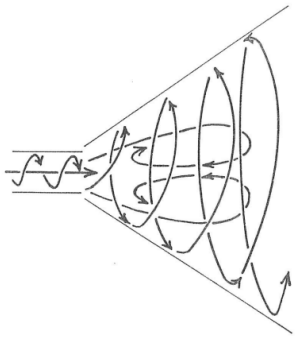

Figure 3.3: Typical Jet Flow with a high degree of swirl. The CTRZ is shown

The size and strength of the recirculation bubble can be controlled by the degree of swirl.

The generation of the CTRZ is explained in [8]: because of the swirling motion of the flow, a radial pressure gradient induced by the centrifugal forces develops in the flow:

$$\frac{\partial p}{\partial r} = \frac{\rho w^2}{r} \tag{3.5}$$

If an atmospheric jet flow with a degree of swirl is considered, the pressure in the axial direction can be calculated by radially integrating Eq. 3.5. As the swirl velocity w decays moving downstream, an adverse pressure gradient is generated in the axial direction. At high swirl numbers, the gradient is sufficient to cause an inversion in the velocity profile.

3.2 Swirl Flows Applications in Hybrid Rockets

Introducing swirl flows in HREs is one of the most common ways to tackle the low regression rate levels of this type of engine [2]. Commonly, swirl is generated using specifically designed injection plates, that give a rotating motion to the oxidizer

that flows into the chamber.
Yuasa et al. developed a GOX-PMMA hybrid rocket with swirling injectors placed at the head end of the cylindrical grain. The regression rate was reported to be 2.7 times higher than that with the axial injection configuration [9].
They also verified the regression rate still follows $r_m = AG_{ox}^n$ even for swirl injection, as only the coefficient A shows an almost linear dependence from the swirl number.

The increase of the averaged regression rate is mainly due to the reduction of the thickness and the growth of the boundary layer, thus enhancing the convective heat transfer [2]. The swirl configuration also increases the residence time of the oxidizer in the chamber, aiding the combustion process.

With the adoption of head-end swirl injection, the local regression rate increases in a zone that is near the injection plate [10]. This is shown in Fig. 3.4.

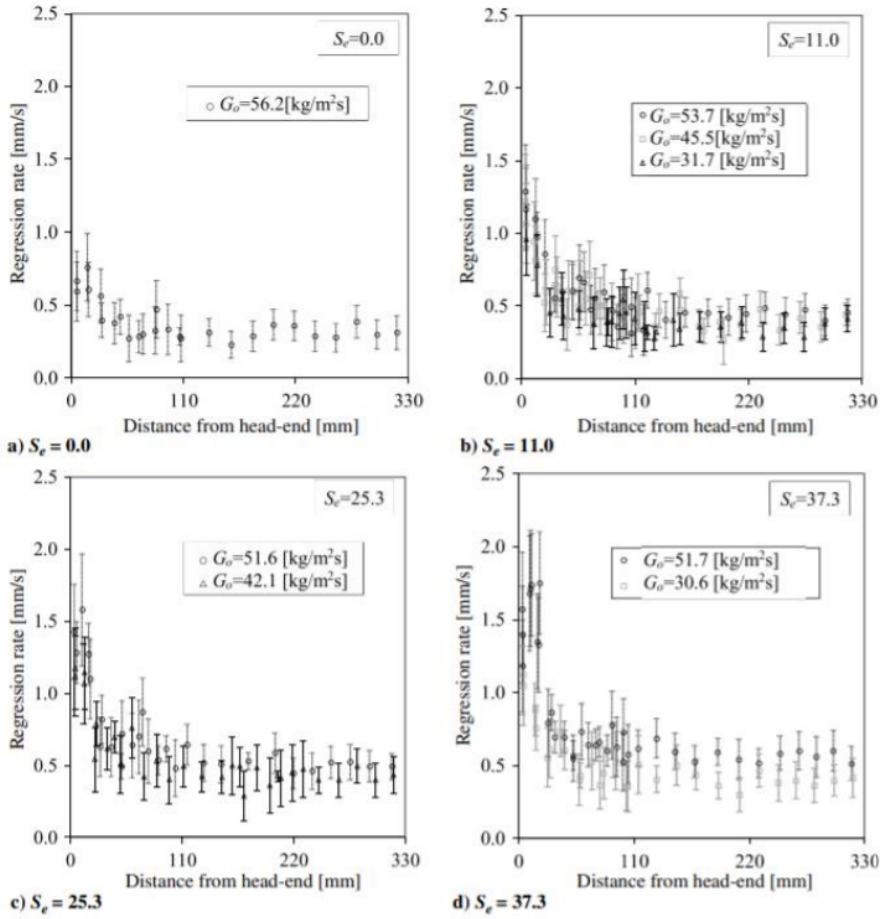

Figure 3.4: Regression rate distribution with different oxidizer flux values [10]

The increase is due to striated swirling flames that adhere to the grain surface, increasing the heat flux. In the nozzle-end, however, these streaks are lighter, suggesting that the flame is detached from the grain wall, thus the lower regression rates.

These results are of interest for this project, as they highlight the fact that the swirling motion imposed by the injectors tends to decay rapidly with the increase of the distance from the head-end, especially for low swirl intensities. Given that the scope of this work is to obtain a more uniform regression rate in the axial direction, it's key to find a way to sustain the swirling motion for the length of the chamber, so that even the nozzle-end can obtain higher levels of regression rate.
In the next section, flow behaviour in spirally fluted tubes (that are a good representation of swirling flows in heated cylinders) is presented as a ground base to understand how to maintain swirling motion in the combustion chamber.

3.2.1 Spirally Fluted Tubes

In [11], Lee at al. use results for spirally fluted tubes to design a grain geometry that aims at sustaining the swirling motion of the flow in the second half of the hybrid rocket motor. The same approach will be used in this project.

Spirally fluted tubes (Fig. 3.5) improve the heat transfer rate by inducing swirl to the flow, disturbing the boundary layer on the surface by repeated flute geometries. This kind of tubes have excellent heat transfer performances with limited flow resistance increase.
The heat transfer capability of fluted tubes is further enhanced by the generation of secondary flow and other vortexes due to the centrifugal forces imposed on the flow.

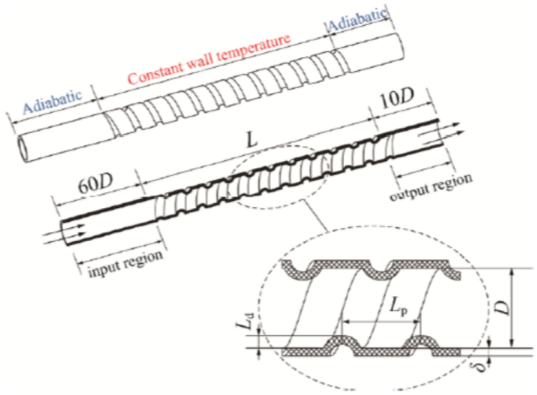

Figure 3.5: Example of a spirally fluted tube used for tests in [12]

Wang et al. [12] observed that as the pitch reduces (the number of spirals on the tube wall grows), the swirl flow is weakened due to the flow transitioning into a more turbulent state, and the heat transfer phenomenon is governed by the turbulence level in the flow.
The swirling generated by the spiral flow is magnified with the increase in pitch, because it weakens the influence of the surface mutation. These results can be seen in Fig. 3.6.

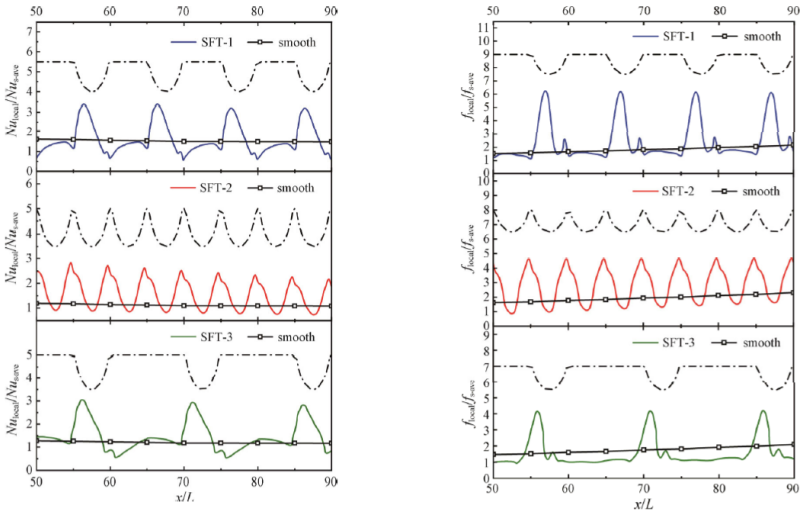

a) $Nu_{local}/Nu_{s\text{-}ave}$ for spirally fluted tubes with different L_p/D (Re=13 300)

b) $f_{local}/f_{s\text{-}ave}$ for spirally fluted tubes with different L_p/D (Re=13 300)

Figure 3.6: Effects of pitch on spirally fluted tubes heat transfer

In another study [13] the effects of groove depth and pitch are considered for a turbulent regime. Different helical pitches and groove depths were tested.
In this study the flow inside the spirally fluted tube was re-constructed through numerical methods. The flow structure can be divided in two types (shown in Fig. 3.7):

- Main swirl flow, found at the core of the tube.
- Secondary swirl flow, found on the groove surface.

It was found that the depth of the groove is an important factor to generate the vortex flow and hence the secondary flow as it affects its strength and intensity; the secondary flow is not present for lower values of groove depth.
The secondary swirling flow is key to this project's topic, as it disturbs the thermal boundary layer, leading to enhanced heat transfer rate and thermal performance [12, 13].

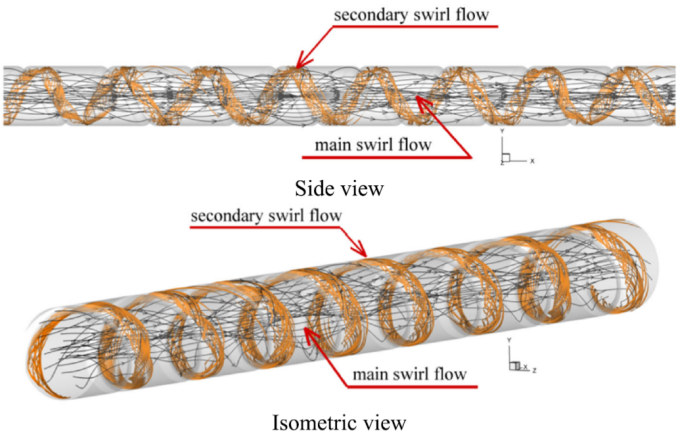

Figure 3.7: Swirl flow structure for a spirally fluted tube

Both swirling flow and the strength of the flow (directly correlated to the Thermal Kinetic Energy distribution) have a direct influence in heat transfer enhancement, so having a moderate groove depth is key.

Chapter 4

CalPoly's HRM Test Facility

From the early 2000s, the Department of Mechanical Engineering at the California Polytechnic State University (CalPoly), San Luis Obispo, has developed a testing facility for a lab-scale hybrid rocket.
In this chapter, the test facility is presented and then the focus is shifted to the instrumentation and data acquisition system refurbishment.

4.1 CalPoly's HRM

The rocket, shown in Fig. 4.1, is capable of developing axial thrust up to 500 lb_f and was primarily designed to test aerospike nozzles and their cooling systems.

Figure 4.1: HRM at CalPoly's Engines Lab

The facility adopts a self-pressurizing system for the liquid oxidizer, exploiting the high saturation pressure at ambient temperature of the Nitrous Oxide N_2O. For this reason it doesn't require a turbopump to pressurize the oxidizer. The oxidizer is stored outside of the laboratory in a dedicated storage area (Fig. 4.2) and connected to the test stand via a plumbing system.

Figure 4.2: Hazardous materials shed containing the N_2O tanks

The rocket setup is the following:

- Pre-chamber and Injection plate. In this portion, up to 12 injectors can be mounted; in 2019 a previous student developed swirl injectors for the system [14]. The injectors are simple 10-32 HexHead bolts with a through hole and various hole diameters can be used to obtain the desired oxidizer mass flow.

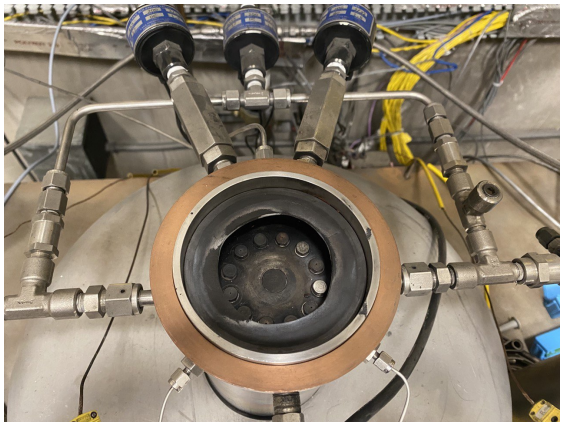

Figure 4.3: HRM pre-chamber

As shown in Fig. 4.3, the fluid lines for the oxidizer and the ignition gasses

(oxygen and propane) connect to the pre-chamber. Each line is fitted with solenoid valves and check valves to prevent flow return.
Two thermocouples are used to read the pre chamber temperature, and one pressure sensor measure the pressure.

- Combustion chamber. The fuel grains are placed inside the combustion chamber casing made of stainless steel. Between the fuel and the casing, a phenolic tube is placed to protect the motor from the high thermal fluxes of the reacting flow.

- Nozzle. In the nozzle the exhaust gases at high enthalpy content are accelerated to supersonic speed. The following figure shows the CAD for the nozzle used for this project.

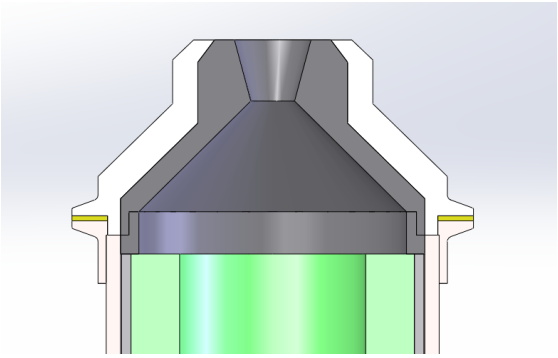

Figure 4.4: CAD of the HRM nozzle

The tree parts are mounted together using banjo clamps, torques to 100 in/lb using a torque wrench.
The following table summarizes the motor relevant dimensions.

Item	Dimension	Unit
Cumbustion Chamber Internal Diameter	8.6	cm
Combustion Chamber Length	29.4	cm
Type 1 Injector Diameter	0.635	mm
Type 2 Injector Diameter	0.762	mm
Swirl Injector Diameter	1	mm
Nozzle Throat Diameter	1.33	cm
Nozzle Exit Diameter	2.4	cm

Table 4.1: HRM relevant dimensions

4.1.1 Hybrid Rocket Ignition Sequence

This section reports the steps followed during the test campaign. After the safety and instrumentation checks were concluded, the rocket could be ignited.

The rocket motor is ignited using oxygen and propane through a dedicated flow control unit outside the test cell. After opening the gasses tanks, two valve for each species (a main valve and a metering valve - green and red for oxygen and propane respectively in Fig. 4.5) are manually operated to obtain a stoichiometric mixture into the pre-chamber that is lit by turning on the spark plug via the *LabVIEW* interface.

Figure 4.5: Rocket Ignition Flow Control Unit

Once a burn on the grain has established (this can be checked by monitoring the pre-chamber temperature), the main N_2O ball valve is remotely opened to allow the oxidizer to flow into the chamber. The valve opens slowly (around 5 s) so that the risk of extinguishing the flame is reduced to a minimum.

After the desired burn time has passed, the N_2O ball valve is remotely closed shut and N_2 is flowed into the chamber to stop the grain from burning. After this process the feed system is purged and/or vented.

4.2 Instrumentation and Data Acquisition System

The hybrid rocket test facility is equipped with various types of instruments, used to acquired the desired data during tests. A considerate portion of the work spent on this project revolves around the re-calibration and refurbishment process that was necessary to bring the lab at an operational state after 5 years of hiatus.

4.2.1 Communication between DAQ and LabVIEW

The first step for this process is to understand how the *Advantech* Data Acquisition System (DAQ) and the main computer communicate via *LabVIEW*.
The DAQ (Fig. 4.6) consists in multiple *Advantech ADAM series* modules: the main module (*ADAM 5000/TCP*) manages the connection between the DAQ, sensors and main computer sending requests and responses to the relevant modules; two relay modules (*ADAM-5069*) that send an activation/deactivation signal to the individual relays when needed; five analog input/output modules (*ADAM-5017UH*) that are used to acquire sensor data and send it to the main computer.

Since the software and the DAQ are from different companies, it was not possible to use most of *LabVIEW*'s express and simplified commands (such as the thermocouple reader), but ad hoc virtual instruments (VI) needed to be created for the majority of the uses that the project needed [15].

The two terminals communicate via a TCP connection over an ethernet cable, using the modbus protocol. This means that whatever voltage the DAQ's Analog Input/Output module (Fig. 4.6) receives, it will be translated in a 12-bit integer value (0 to 4095) and then transmitted to be visualized in *LabVIEW* [16].

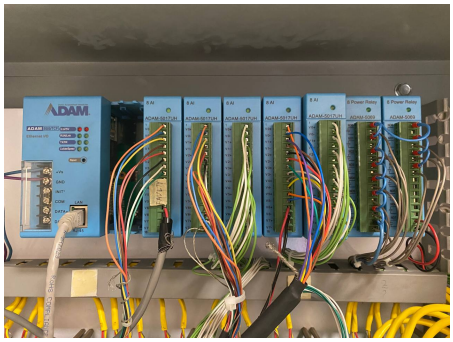

Figure 4.6: Engine's Lab DAQ. The 5017 UH module are A/I and are connected to the sensors. The 5069 modules (last two on the right) operate the relays

It's then extremely important to correctly scale the integer values in order to accurately read the sensors measurements. Various manuals were consulted for this purpose [17, 18].

4.2.2 Thermocouples

Thermocouples (TC) are electrical devices consisting of two dissimilar electrical conductors that form an electrical junction. They produce a temperature-dependent voltage exploiting the Seebeck effect; the voltage can then be interpreted to measure temperature.
The TCs at Cal Poly's engines lab are *Omega Type K thermocouples*, the most common type. They have a general temperature range of $-200°C$ to $1260°C$ and they output 0.000 mV at $0°C$. They are connected to the DAQ through amplifier boards (Fig. 4.7), used to boost the voltage output of the sensor (that otherwise would be in the order of the milliVolts, too low to withstand the cable distance between DAQ and computer) to a voltage that the Analog I/O module can process (0 to 10 V).

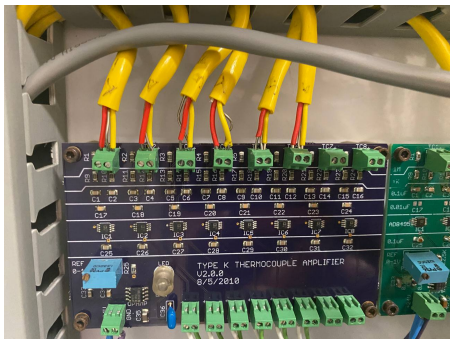

Figure 4.7: TC Board 1 in the DAQ case

The first key activity was to check the TC channels for the new DAQ configuration via *LabVIEW*. In order to do so, the following procedure was employed:

- The ad-hoc *Labview* VI for TC communication is started.
- A thermocouple wire is connected to the *FLUKE 714 THERMOCOUPLE CALIBRATOR*.
- The calibrator is set in OUTPUT MODE to simulate a thermocouple reading; this step was preferred instead of simply putting a finger on the TC because it is less time consuming and because it allows to simulate bigger changes in temperature (and consequently voltage) that are easier to track on the interface.

- For every channel, the simulated temperature is varied in order to track differences of integer value detected by the VI. The process is repeated until a channel displays an actual change in value.

The various TCs were then labeled with the current channels and an updated excel file was created to keep track of changes.

Thermocouples Calibration

Type K thermocouples' output voltage does not follow a linear trend with temperature, as shown in Fig. 4.8. It was then necessary to use more than two calibration temperatures (freezing water at $0°C$, and boiling water at $100°C$) in order to obtain an accurate trend to translate the integers values into temperatures.

During a first calibration attempt it was found that the first thermocouple amplifier board (named TC board 1) didn't work well with temperatures below $120°C$ (the lowest measurable temperature was $-35°C$, not compatible with the predicted N2O temperature in the main line).

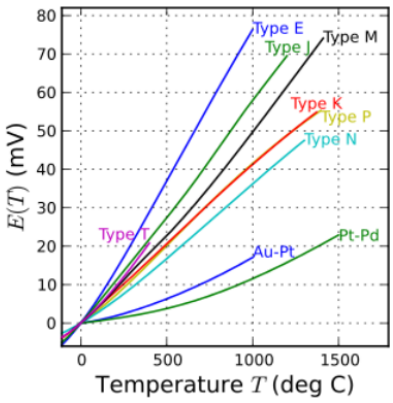

Figure 4.8: Characteristic Curve of most thermocouple types

After assessing that the calibration process followed was correct, in order to solve the issues of non-linearity and low temperatures accuracy the following solutions were adopted:

a) A non-linear fitting was implemented to improve the overall accuracy of the TCs. It was found that Terry Cooke (the student that set up the DAQ system in the late 2000s) used non-linear fitting curves during the setup of the facility.

b) To solve the issue with low temperatures, TC Board 2 was also calibrated.

TC1 was connected to this board using a new TC wire as an extension of what was TC 7.

The two TC boards were calibrated to different temperature ranges, so that they can be more accurate in the predicted ranges they will experience during their operations. It was decided to use these ranges:

- For TC Board 1: temperature from 0 to 1200 $°C$ with 100$°C$ increments. Integer values were collected in an excel table.
- For TC Board 2: temperature from -200 to 40 $°C$ with 20$°C$ increments.

The calibration output curves and their relative "translation equations" are displayed in Fig. 4.9.

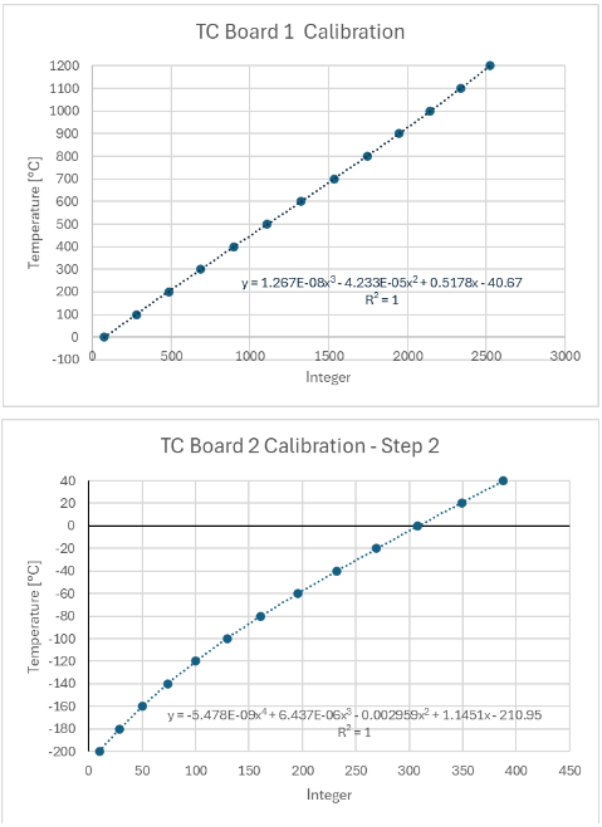

Figure 4.9: Calibration curves for the two amplifier boards

A simple *LabVIEW* subVI was then created in order to translate the integer values to temperature that would be later called in the test interface VI. Writing the VI

in this manner also simplifies the changes needed to read multiple TCs at the same time.

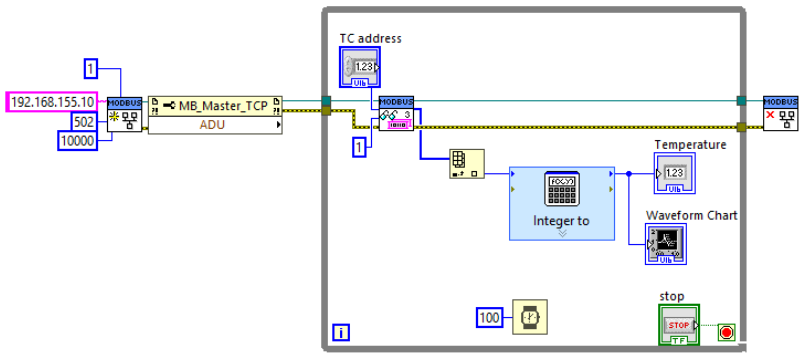

Figure 4.10: *LabVIEW* Virtual Instrument for TC readings

4.2.3 Pressure Sensors

A pressure transducer (PT), often called a pressure transmitter, is an electromechanical device designed to measure pressure with a high degree of accuracy. Pressure transducers sense applied pressure and output an electrical signal by using a combination of mechanical and electrical components. The most common transducer outputs are voltage and milliamps.
The PTs at Cal Poly's engines lab are *Validyne Engineering DP15 - Variable Reluctance Differential Pressure Transducers*, a particular type of sensor, with the output in the range of the Volts (20 mV/V full scale typical - per their datasheet); they are differential pressure transducers, so they return measurements of gauge pressures.

Prior to calibration, each PT was checked for proper functionality according to Validyne Engineering specifications [19]. The parameters checked were:

- For Continuity: using a multimeter on low resistance, it was checked that the resistance between the pins with white and black wire respectively was around 60 Ω. If an "open circuit" reading is returned the sensor needs to be changed.

- For Isolation: the resistance between black wire pin and sensor body; using the multimeter at his highest resistance setting, it was checked if a value higher than 100 $k\Omega$ (or open circuit) was showing.

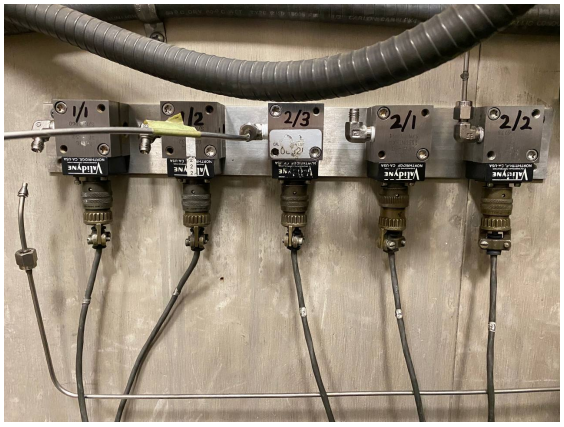

Figure 4.11: Pressure Transducers on their mounting bracket in the test room

- Corrosion: the sensor body was opened and the diaphragm and O-rings were checked for corrosion.

To identify the correct DAQ channels a similar procedure to the one for TCs was followed.

Pressure Transducers Calibration

The PTs are connected to the DAQ via a *Validyne Engineering CD-280 Dual Carrier Demodulator*, a device that provides a DC signal that - once calibrated - will be proportional to the pressure at the transducer.

Figure 4.12: Demodulator that connects PTs to DAQ. The two holes for each channel hide the screws that are used to adjust gain and zero for each sensor

The calibration is done as a system (transducer, cable and electronics together) and must be done when all the components are connected together.
Calibration adjustments for Validyne sensors involve two parameters: zero and

span/gain. These adjustments will be done by working on the carrier demodulator. The manufacturer suggested calibration procedure was followed:

- The zero screw was adjusted so that a voltmeter would read $0V$ when a pressure of 0 *psig* was applied.
- The gain screw was adjusted so that a voltmeter would read $10V$ when a pressure of 800 *psig* was applied

In order to obtain said pressures, a N_2 tank was connected to the sensors and regulated to the desired pressure. It's important to note that the maximum pressure that a sensor can withstand is given by the specific diaphragm mounted on it (the rocket PTs mount a 3-60 diaphragm, capable of measuring up to 1200 *psig*).

The sensors have a linear behavior with pressure so, after having assessed the linearity, only three points (zero, mid and full scale) were used to obtain the curve necessary to translate the integer value to a pressure for each PT. The result is shown below.

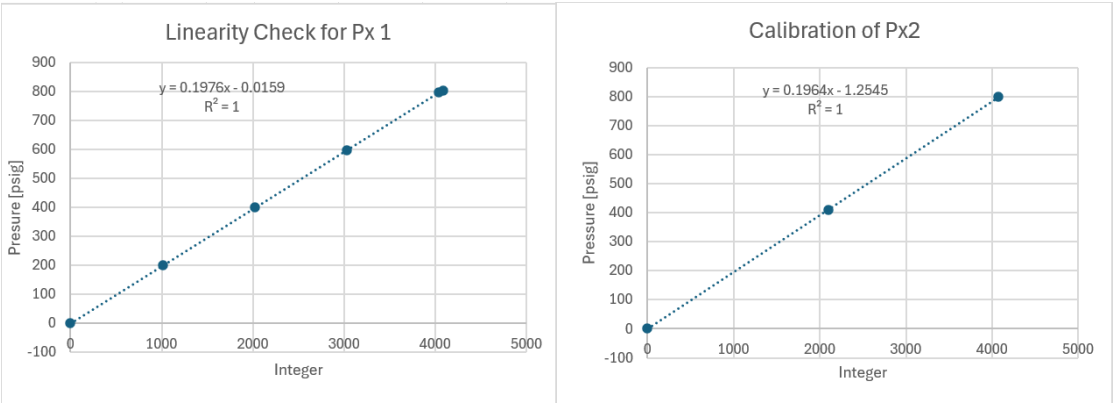

Figure 4.13: Curves for PTs

4.2.4 Relays and Valves Operations

The valves in the rocket assembly are connected to the DAQ through relays, that boost the voltage received to the items thanks to an external power supply. Relays are considered coils in the Modbus architecture, so they accept only boolean inputs as data.
Being able to communicate correctly with these elements is therefore a key aspect in order to be able to automate the test process.

A very simple *LabVIEW* script, used to assess the actual channel for each individual coil, is presented in Fig. 4.14. This was used not only to check the channels, but also to check the operability of the instrumentation connected to each relay (valves, spark plug, etc...).

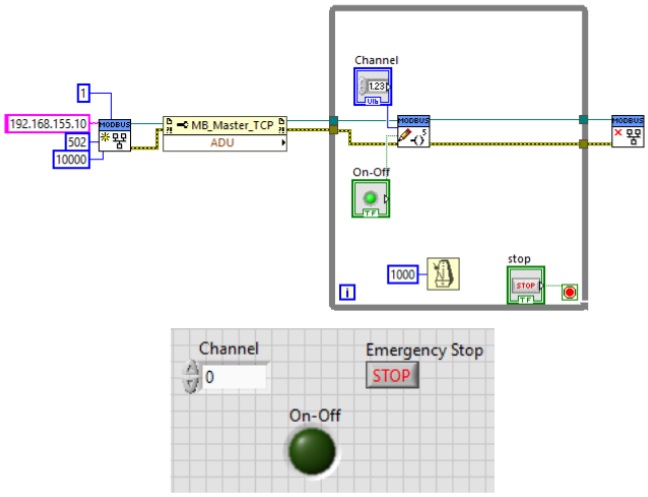

Figure 4.14: Script for relay activation. The *write single coil* block is used to send a boolean input to the desired channel and consequently to the relay. In the lower part, the user interface is shown

To check the operability of each relay, it was checked that the light on the relay (Fig. 4.15) turned on when the toggle position in *LabVIEW* was on. At the same time, to check if valves and spark plug were functioning properly, it was sufficient to wait for a clicking (or repeating for the spark plug) sound when the relay connected to a valve was flipped on.

During this phase, it was also found that in order to properly activate the relays so that they can output the correct power to the instrumentation (12 V) the *main power* relay has to be turned on, otherwise the relays on their own wouldn't give enough power to operate the valves. The "main power" relay serves to activate the electrical connection between the power source.

Main N2O Valve Operation

Of the instrumentation present in the test room, one of the valves (the ball valve that controls the flow on the main N2O line, reported in the Fig. 4.16) is not

Figure 4.15: Relay box in the DAQ. The figure also shows the input and output cable arrangement

activated directly via relay, but through a *Nucleo Board* (a micro Python processor) that controls a DC motor through a custom script.

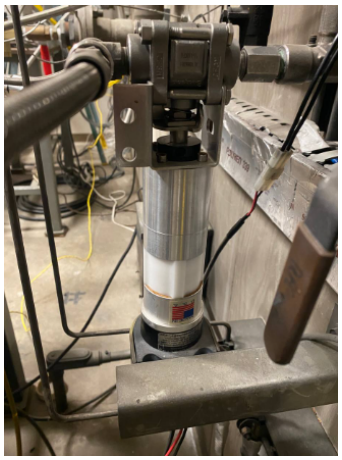

Figure 4.16: Main N2O valve with the DC motor connected at the bottom. The wires that connect the motor to the *Nucleo Board* can be seen in the lower part of the Figure

This valve cannot be operated by simply activating a relay as it is necessary to have some degree of control over the opening speed, so as to avoid the flame being extinguished by too much N_2O entering the chamber or for throttling necessity. In order to do this, a Python script was created that allows the creation of a user interface through serial communication with the Nucleo Board via *Putty* (a software for serial communication).

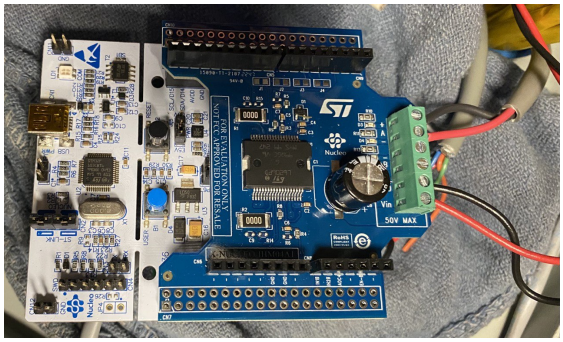

Figure 4.17: Nucleo Board for valve communication. It's connected to the main computer with a active USB cable (and a microUSB adapter) and to the DC motor through a motor driver and electrical wires

The code defines the opening/closing time of the valve and the duty cycles (percentages) for the motor during opening/closing. They are defined as follows:

Operation Time	4.5	s
Duty Cycle Open	60	%
Duty Cycle Close	60	%

Table 4.2: Specification for Main N2O Valve operation

Using these values allows the user to open and close the valve with 2 commands, allowing for a "step" opening, so that the risk of blowing out the flame is limited. The open and close commands are given through keys: O opens the valve, while C closes it.

4.3 Changes in the Set Up During the Project

During the course of the thesis work, various changes to the setup were made as some of the oldest instruments stopped working or broke. The major events and the solutions adopted are reported in this section.

During the checks for the main N_2O valve operations, the coupling that connected the DC motor and the valve broke (Fig. **??**); a new coupling was ordered from the same manufacturer, but the lead time was longer than expected and a temporary solution was adopted.
The solution consisted in removing the motor from the line and forcing the ball valve open using a wrench. After this operation, the N_2O flow was controlled by opening and closing the big ball valve in the tanks' shed; during the tests an

assistant was needed to open/close the valve from it's control box outside the test cell. The biggest drawback from this solution was the fact that precisely controlling the burn time for the engine became complicated as it relied on the timing of the person operating the valve.

Figure 4.18: Image of the coupling fracture after the DC motor was removed from the system

Midway through the test campaign, the system power supply broke and a temporary solution was needed as a replacement would arrive too late for the project schedule. A power supply that was already available in the M.E. Dept. was tried, but it could not provide enough current to the spark plug.
The solution adopted was to use an external 12V battery, directly connected to the relay shaft in the DAQ box using electrical wires and pins. The battery was checked for charge level and voltage provided before being connected to the system; afterwards, the test procedure was carried without flowing gasses into the system just to check the correct operability of the valves and spark plug. The battery was then successfully used as the power source for the system.

Chapter 5

Hybrid Rocket Grain Design

The main drawback of Hybrid Rocket Motors is the low fuel regression rate; nowadays, many methods have been proposed to increase the regression rate of HRMs: some involve the injection of oxidant, others act on the actual solid grain.
Of the second ones, helical grain is a potential novel configuration proposed recently; the presence of helical grooves in the fuel port could induce swirl flow in the combustion chamber and enhance diffusion and mixing of the oxidizer and the fuel pyrolysis gas [20].
Besides, the helical structure is not complex and the grain can be simply manufactured using conventional methods or 3D printing. This type of configuration is also suitable to small-scale attitude control HRMs.

The combustion flow field characteristics of this type of grain are still not clear, as few research studies have been carried out to date. In an attempt to better understand the design process for the helical grain, the literature research for this project didn't stop at HRM [11, 20, 21, 22, 23] but various fields of study were investigated, such as heat transfer in cylindrical channels [24], flow entrainment in grooved channels [25] and more.

5.1 Geometric factors influencing the fuel regression rate and fluid flow

The geometric factors that influence the fuel regression rate of the helical grain can be summarized as thread pitch, groove depth, groove width [20] and groove shape.

To understand how these factors influence the regression rate of the grain Tian et al. [20] adopted the Taguchi orthogonal method; this testing method allows to study the relationships between different factors that influence a phenomenon and

to identify which are the most important, by carrying out a limited number of tests. Various tests were conducted with varying values for pitch, groove depth and groove width (the groove shape was not investigated in the study) as summarized in Table 5.1. All the parameters except for the oxidizer mass flux are reported in dimensionless values ($parameter = Param/IntDiam$) so that they can serve as a starting point for this project's design.

Parameter	Value 1	Value 2	Value 3
Oxidizer Mass Flux $[g/s]$	300	100	150
Thread Pitch	0.75	0.45	1.5
Groove Depth	0.05	0.10	0.15
Groove Width	0.20	0.25	0.30

Table 5.1: Geometrical Parameters values in the research considered

The authors investigated the degree at which every parameter influences the phenomenon by calculating the range of the regression rate R:

$$R = max\{K_1, K_2, K_3\} - min\{K_1, K_2, K_3\} \tag{5.1}$$

where

$$K_i = \sum_{j=1}^{3} r_{avg,j} \tag{5.2}$$

and K_i is the sum of the simulated regression rates corresponding to the indicator i.
The results show that of the geometric factors, thread pitch plays the most important role in enhancing the regression rate, while groove width is the least important, as shown in Table 5.2.

	$\dot{m}_{ox}$	B	C	D
R	0.627	0.081	0.060	0.039
chief $\rightarrow$ minor	$\dot{m}_{ox} \rightarrow B \rightarrow C \rightarrow D$			

Table 5.2: Degree of influence of the different factors involved in the study, where B: pitch, C: groove depth, D: groove width

In the following sections more results about the geometric parameters are investigated.

5.1.1 Effects of Groove Shape

Groove shape is important because it allows for the correct flow entrainment that can lead to better heat exchange capability, as the grooves act as periodic disturbance promoters along the stream-wise direction, as for the spirally fluted tubes discussed in section 3.2.1.
The grooves help create a swirling motion in the flow field; when this occurs, the velocity and thermal boundary layers on the wall become thinner and the heat transfer in that region will be augmented [24].

A study by Bilen et al. [24] investigated the groove geometry effect on heat transfer; three different types of grooves were investigated: circular, rectangular and trapezoidal. The grooves dimensions were the same for each type (as shown in Fig. 5.1), with the only difference being that the pitch for the trapezoidal grooves is longer than that of the other two because of geometric limiting factors.

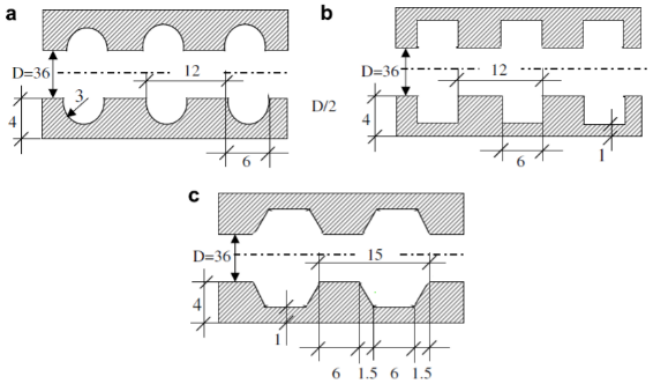

Figure 5.1: Different types of grooves analyzed by Bilen et alles

The groove depth was set at 3 mm (0.0833 ID) and the length was set at 6 mm (0.167 ID).

During the tests it was found that the main fluid mechanism that enhances the heat transfer performance is the intensification of the fluid mixing by the grooves. Results show that the tube flow with different grooves configurations causes a significant increase in the heat transfer rate (Fig. 5.2).

It was also found that the increase in Nusselt number (related to pressure drops) is more pronounced in the circular groove, while the heat transfer enhancement is similar between the trapezoidal and circular grooves (63% for circular and 58% for trapezoidal, with rectangular grooves at 47%). The heat transfer rate for the trapezoidal groove approaches the value for the circular groove with 20% less

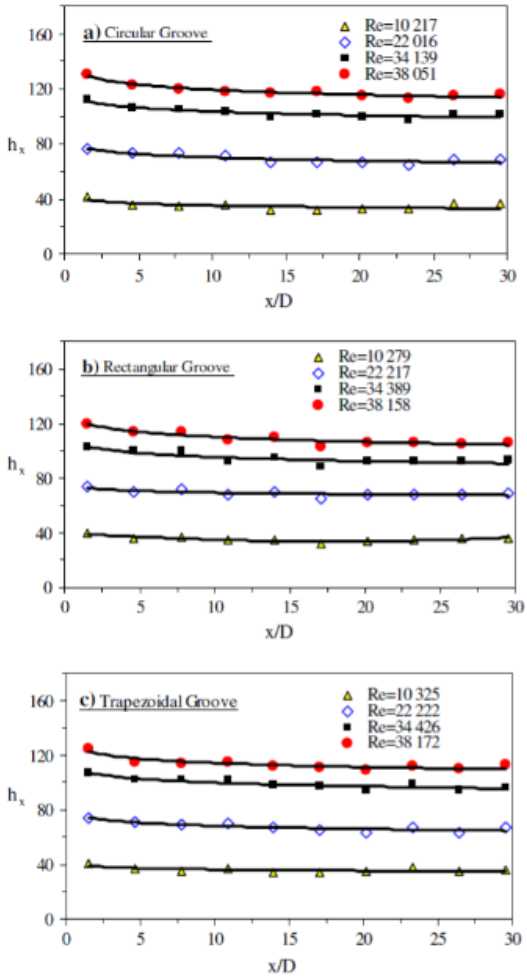

Figure 5.2: Effects of groove shape on heat transfer rate over different Reynolds Numbers

grooves in the pipe (due to the longer pitch).

The circular and trapezoidal grooves can also reduce the presence of recirculation zones, providing more surface sweeps by avoiding a sharp vertical corner in the flow path. This causes beneficial disturbances in the flow and results in better heat transfer.
After analyzing the results it can be hypothesized that using grooves provides heat transfer augmentation, due to various reasons such as:

- producing more turbulence;
- better fluid mixing;

- increase in the heat exchange area;
- periodic redevelopment of the boundary layers.

A closer inspection of the results helps to compare the different geometries. The circular grooves have better performances (7%) than the rectangular ones, due to a better fluid mixing, given that they have the same pitch. Circular grooves have only a 3% increase in performance with respect to the trapezoidal type, even if the second one has a lower number of grooves. So it can be said that trapezoidal grooves are able to obtain a similar mixing and heat transfer area to circular ones even with longer pitch.

From this analysis it's clear that for the HRM project the choice falls between circular and trapezoidal grooves.

5.1.2 Effects of Thread Pitch

Thread pitch is the most important geometric factor in the heat transfer augmentation provided by helical grooves [20]. It is then key to understand how it influences the flow field and heat transfer performance in the combustion chamber.
Most of the research that has been carried out for this configuration involves axial injection of the flow into the test chamber, while only a few articles consider pre-existent swirl flow before the helical section [21, 22, 23]. The results without swirl flow were analyzed in order to understand the basic effects of pitch on the heat transfer and flow entrainment capabilities of the helical structure; the results that also involved swirl flow were then used as baseline to select a helical pitch for the project.

Effect of pitch without swirl flow

Studies with varying pitch and constant groove parameters (depth, width) were mainly taken into considerations; all the dimensions are reported as multiples of internal diameter so that an easier comparison between different studies can be made.

A study by Mogaji [25] states that the enhanced surface geometry of grooved tubes affects the rate of heat transfer significantly. In these tests, pitches in the range of 1 to 5 internal diameters were analyzed, with the better performance obtained with the lowest pitch considered (125% increase in heat transfer rate); similar performances were observed for p/D of 3 and 5 (about 80% increase).
The results are in accordance with other studies, but only serve as a qualitative standpoint as the working fluid used was water, that is too different property-wise

with respect to the fluids that will be adopted for this project (N2O and PMMA fuel).

Other studies, such as Leet et al. [11, 21, 22, 23], considered a helical grain for HRMs. They considered pitch ranges from 0.15 to 5 internal diameters when implementing axial injection for the oxidizer. The fuel used was PMMA and the oxidizer was GOX. The rocket motor tested was 20 cm long with a 2 cm ID.
The pitches tested are reported in Table 5.3.

Pitch	0	0.15	0.30	0.60	0.90	5.0
Charg. Vol	100%	98.94%	99.09%	99.18%	99.39%	98.49%
Surface	100%	149.3%	137.8%	116.8%	111.9%	136.1%
Vol. Burn. Rate	100%	135%	120%	116.4%	99-101%	114%

Table 5.3: Grain characteristics for the grains analyzed by Lee et al.. The pitch here is reported as a dimensionless value obtained by dividing by the internal diameter

The regression rate trends for most pitches are reported in Fig. 5.3, as well as the configurations used.

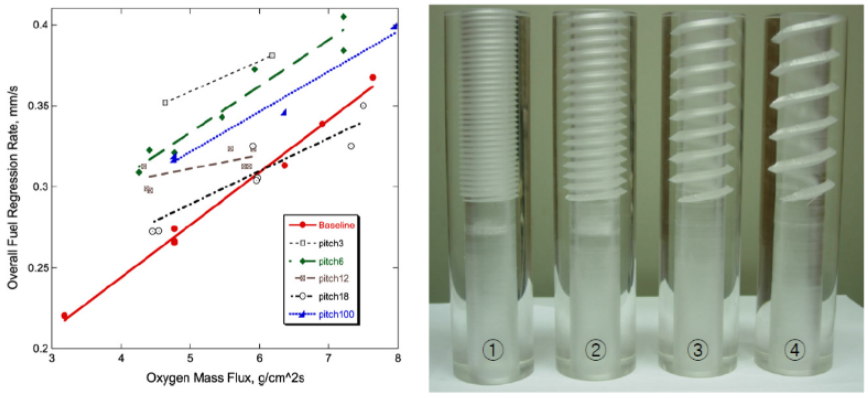

Figure 5.3: Results obtained in the studies by Lee et al. On the right, the different grains for pitches from 0.15 to 0.90 are shown

The tests show that without swirl, a fuel with smaller pitch is more effective in increasing the regression rate of the fuel.

Effects of pitch with swirl

It's important to understand the changes in performances brought by the presence of initial swirl in the flow field, especially for the scope of this project which is to

obtain a better and more uniform regression rate along the grain.

Lee et al. investigated the matter by comparing two different helix configurations (6 mm and 100 mm - corresponding to 0.3 and 5 internal diameters) when a swirl injection with S=3.71 was adopted. The results obtained are reported below.

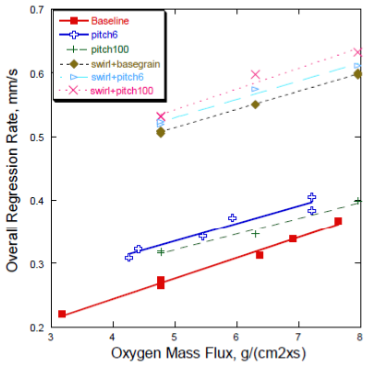

Figure 5.4: Results on the regression rate with the configurations tested

As it can be seen, when swirl is imposed on the flow, a higher pitch gives better increase in regression rate. This is due to the fact that there are two main mechanisms that concur in the enhancement of heat transfer and so regression rate:

- Inducing swirl into the bulk flow; related to the space between the adjacent grooves (pitch) and their depth.
- Inducing turbulence; determined by the helix angle and the pitch.

The pitch is the key parameter in determining which mechanism is taking place: if the space between the flutes (grooves) becomes smaller, they act like a turbulence generator rather than to induce swirl to bulk flow [21]. Fig. 5.5 shows how different pitches favor different enhancement mechanisms.
If swirl is already imparted into the flow (e.g. by adopting swirl injectors) it's better to opt for a higher pitch than a lower one, as it can help sustain the swirling motion in the flow field.

Another important factor in the combustion chamber is the pressure profile as it heavily influences the combustion efficiency and thrust generation in the HRM. When combined with an initial swirl source, higher pitches tend to have more uniform pressure profiles than lower pitches and a less pronounced pressure drop, as seen in Fig. 5.6.
Thus, it can be summarized that a configuration with large thread pitch could achieve an optimal condition for a maximum in regression rate if combined with

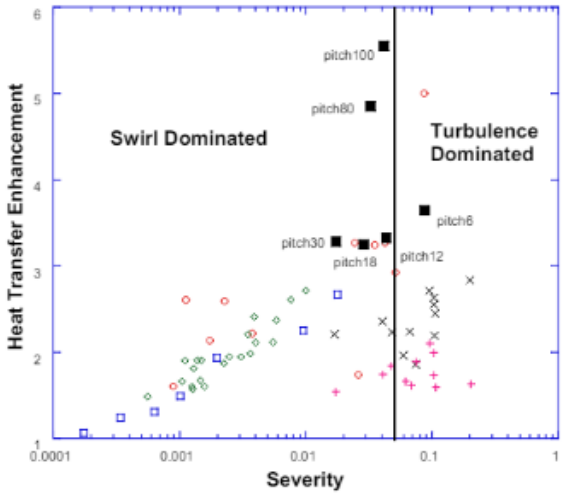

Figure 2. Heat transfer rate enhancements in spirally fluted tubes

Figure 5.5: Heat transfer enhancement plotted against the severity, a parameter that accounts for the characteristics of the grooved tube (width, pitch, diameter)

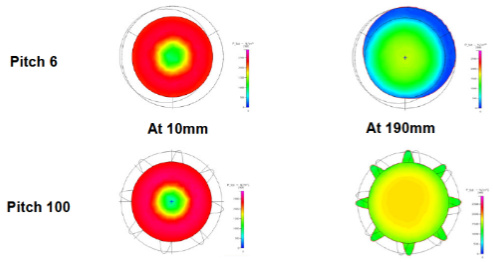

Figure 5.6: Total pressure distribution at two different axial locations. It can be seen that the bigger pitch shows a more homogenous profile

initial swirl [22].
Unfortunately in [23], no attempt in finding the optimum swirl strength was carried, so a particular level of attention needs to be adopted in the design phase.

5.1.3 Effects of Groove Depth

The groove's depth (e, e/D) is also an important geometric factor when interested in the heat exchange performance; it also plays an important role in flow entrainment rate together with the groove shape.

Not many studies analyze configurations that are comparable in size to the project. The few results that can be used as a baseline ([20, 24, 25]) all agree on the fact

that increasing the groove depth leads to an increase in regression rate, probably due to the fact that flow is trapped in the groove and has a lower escape rate if the walls of the grooves are higher.

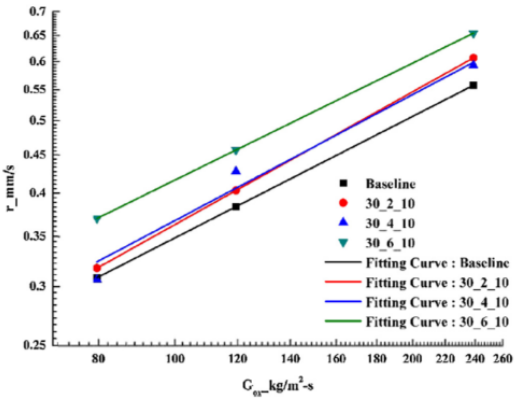

Figure 5.7: Effect of Groove Depth e on the regression rate

An important aspect to take into consideration when applying grooves to solid grains in HRMs is that when grooves are too deep there is a risk to increase the percentage of residues and slivers once the combustion process is finished. It is then important to not increase the depth too much.

5.1.4 Effects Effects of groove width

Fig. 5.8 shows the average regression rate of the helical configuration with different groove widths [20]. It can be seen that the presence of grooves increases the regression rate and that the average fuel regression rate increases with the increase of width.

It can be seen that the enhancement is less important than that obtained with other geometric parameters, and that a groove width too small can be detrimental for lower oxidizer mass fluxes.
By comparing the burnt samples (Fig. 5.9), it was found that excessively wide grooves would decrease the regression rate at the upwind side of the concave part of helical grain. This would lead to a non-homogeneous regression rate along the grain and the presence of residues that are to be avoided for the scope of this project. Then, it's important to choose the groove width inside a reasonable range, so that their positive effects are not overturned.

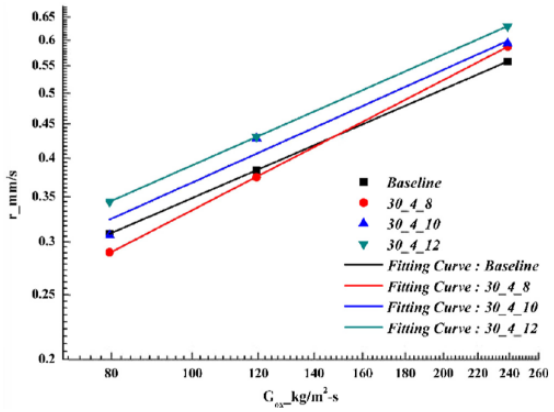

Figure 5.8: Effect of Groove width w on the regression rate

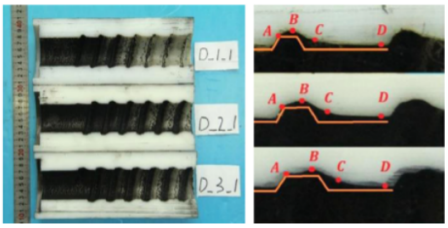

Figure 5.9: Burned samples for groove width effect comparisons

5.2 Helical grain geometric features design

After understanding how the different geometric features of the helical configuration influence the objectives of this project, the results can be used to properly design a solid grain for Cal Poly's Engine Lab hybrid rocket motor.
In the following sections, the choices made for each feature of the helical grain are reported.

5.2.1 Thread pitch design

After analyzing the results displayed in section 5.1.2, it was decided to choose a longer thread pitch because swirl injectors are adopted for the HRM.
To design the appropriate pitch the results for the studies that considered helical grain and swirl injection [11, 22] were plotted in order to search for a trend in the regression rate enhancement with helix pitch (Fig. 5.10).
For all the oxidizer mass fluxes the regression rate seems to reach a maximum and then decrease, with the maximum (dimensionless) values at pitch 2.7, 2.7 and 4.0 respectively. These values could have been used as baseline for the design of the project but were disregarded due to the low amount of points available to find the

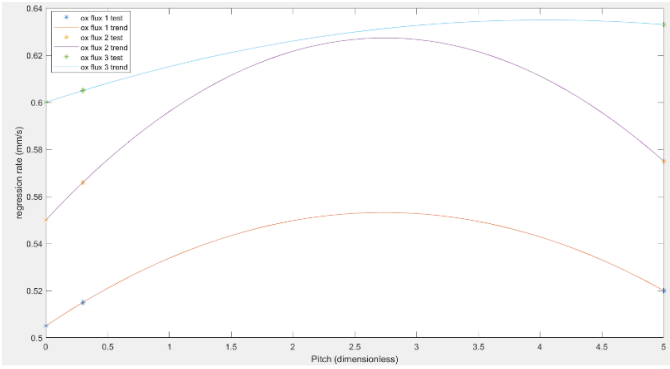

Figure 5.10: Plot for regression rate prediction at oxidizer mass flux of 4.75, 6.25 and 8.00 g/cm^2s respectively

trend and the prominent gap between the two pitches considered in the studies.

After further analysis of the design process adopted by [22], it was found that the adimensional value of pitch 5 (100 mm in their case study) was selected after having calculated the swirl number imposed by the injectors to the flow in the upfield section of the grain; the injectors were able to create a swirl number that corresponds to an angle of 30° with respect to the axial direction. The pitch was then built in order to match that angle.
The same process has been followed for this project. The swirl injectors already manufactured at Cal Poly [14] are able to impose a swirl number S=0.115, that corresponds to an angle of

$$\theta = \frac{3}{2}\arctan(S) = 9.84^\circ \tag{5.3}$$

That would lead to a pitch of

$$P = 2\pi r \tan(90 - \theta) = 1014 \quad mm \tag{5.4}$$

This way, the grooves will act as guide vanes for the flow, allowing the maintenment of the swirl across the chamber length and hence a better regression rate in the second part of the fuel grain.

5.2.2 Groove Depth Design

Groove depth design is important as it has a prominent role in flow entrainment. As stated in section 5.1.3 regression rate was found to be increasing with groove depth. The scope of this project, however, is not just to increase the regression rate of the solid grain but also to obtain a more uniform distribution of that parameter

along the grain length, also reducing the presence of residues in the burnt samples.

The maximum depth is limited by the difference between internal and external diameters of the solid grain, that are 58 and 86 mm respectively; this leaves the grain thickness at 14 mm.
Having grooves that are too deep doesn't only imply the presence of residues in post-burn analyses, but also affects the temperature profile along the grain surface. Fig. shows that grooves with higher depth have a less homogeneous temperature profile, rather than grooves with lower depth.

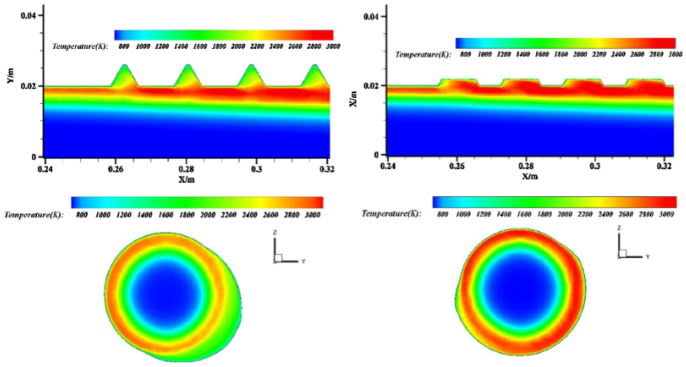

Figure 5.11: Temperature profile for different groove depths

Having a more uniform temperature profile would lead to a more uniform heat transfer rate in the helix section of the grain and consequently a more uniform regression rate. It would also help preserving the thermal protection for a longer period of time, preventing the combustion chamber from being subjected to excessively high thermal loads.

After taking these results into consideration, it was decided to adopt a moderate groove depth of 5 mm, with the aim of having both the positive effects of increasing the depth while trying to reduce post-burn residues at the same time.

5.2.3 Groove Width Design

Groove width is the least important geometric factor to influence the regression rate of the HRM in the helical configuration.
After analyzing what was proposed in section 5.1.4 it was decided to opt for a width that is a compromise between the widths tested in [20] (0.20 and 0.25 internal diameter respectively).

The groove width adopted is 14 mm. This value would also work well with

the theorized thickness of the flow calculated in previous works [26].

5.2.4 Number of starts and length of the helix section

According to multiple sources, the number of helical starts should be equal to (or at least half) the number of swirl injectors present on the injection plate [11, 22, 26]. At Cal Poly's engines lab up to 8 injectors are available (Fig. 6.7), manufactured by students for past projects [14, 26].

For an easier injector assembly procedure (especially for easier pointing angle

Figure 5.12: One of the swirl injectors manufactured by previous students at Cal Poly

determination), it was decided to use 3 or 6 injectors, so the number of starts is 6. The choice of the actual number of swirl injectors used will be discussed later.

The length of the helix section is a key parameter for this project scope. The aim of the helix section is to maintain the swirl motion imposed by the injectors along the grain length. The helix will start when the swirl is starting to decay, so that it can keep the momentum of flow and sustain the tangential motion of the N2O and combustion products.

The injectors were specifically designed to have the oxidizer jet impinge at 9 cm from the port entrance in an attempt to obtain a more uniform regression rate and at the same time avoid the entrance effects that are typically observed with axial injectors. The swirl imposed is very weak and it should decay after a small portion of the grain has been covered; unfortunately, the collegues that machined the injectors couldn't test because of the Covid-19 pandemic hitting the US. In

order to understand where the starting point should be along the grain length, it's necessary to analyze a post-burn sample of the baseline cylinder with swirl injectors and identify the zone where the swirl starts to decay (which from theory and CFD studies [14] should be at about 10 cm from the injection plate).

5.2.5 Geometric features summary

The following table summarizes the design choices made for the geometric features of the helical grain configuration.

Thread Pitch	1014 mm
Groove Depth	5 mm
Groove Width	14 mm
Number of starts	6
Axial position of starting point	120 mm

Table 5.4: Geometric features of the fuel grain to be tested

The starting position was determined after having analyzed a burnt sample, and is discussed later.

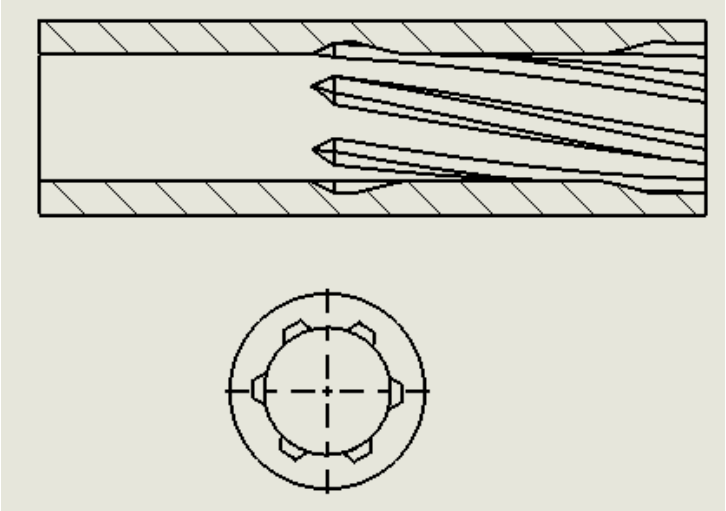

Figure 5.13: Helical Grain geometry in *SolidWorks*

5.3 Fuel Manufacturing

Because of the complex internal geometry of the designed grain, it was decided to opt for 3D printing instead of traditional techniques for manufacturing.
3D printing with PMMA could prove to be a challenge, because most 3D printer companies still consider it an "exotic" material and finding the correct printer settings could require a lot of trial and error.

5.3.1 3D Printing Process

The 3D printer used for this project is a *Bambu Lab X1-Carbon* available at Cal Poly's Aerospace Fabrication Lab (accessible for the purpose of this project thanks to the Aerospace Lab technician). Different test prints were made in order to find the correct settings; after a number of tries and some research online, the settings with the best print result were chosen.

The best print process was obtained after drying the filament for at least 4 hours; this was done because PMMA filament is prone to absorb humidity from the atmosphere. If a high concentration of water is present, when the filament is heated in the nozzle, an uneven flow could be observed, considerably lowering the quality of the print and the ability of the filament to stick to the printer's bed.

For the bed, a texture PEI plate was used. The coarse surface helped solving the sticking problems commonly faced when printing with PMMA. The bed was also heated to $110°C - 115°C$ for better sticking; the temperature had to be modified to account for the atmospheric temperature during the printing process.
The nozzle temperature is also very important, as it determined the quality of the flow while printing. Setting this temperature too low would result in uneven flow, that would make the printed piece too brittle and voids would be present. Setting the temperature too high would cause the nozzle to clog, causing a complete print failure. The nozzle temperature was then set at $250°C$, allowing a smooth PMMA flow during the process.

The printer is equipped with tree different cooling fans, allowing to precisely control the printing chamber temperature. Table 5.5 reports the fan speed settings adopted; it was key to have a decently warm chamber (around $45°C$) as PMMA is likely to warp and/or shrink if printed in a cold environment. For the same reason, the printer's enclosure had to be closed to stabilize the temperature of the chamber.

Print speed is another key parameter for a successful print. PMMA filament is very fragile and requires low print speeds to correctly stick to the bed or to

previously printed layers. Unfortunatly, even though the *Bambu Lab X1-Carbon* is able to print at high speeds (such as 300 mm/s), the best speeds were found to be 40 mm/s for the first layer and 50 mm/s for the subsequent ones. The first layer has to be printed at a lower speed to make sure it sticks properly to the bed.
With the print speeds selected, it took approximately 72 hours to obtain a complete fuel grain.

Print settings for X1 Carbon	
Filament Drying Time	4 h
Infill Density	100 %
Infill Patter	Lines
Nozzle Temperature	250°C
1st Layer Print Speed	40 mm/s
Print Speed	50 mm/s
Bed Temperature	110-115°C
Fans Speed	Nozzle: OFF
	Auxiliary: OFF
	Chamber: 40%

Table 5.5: 3D print manufacture settings. The bed temperature is adjusted while the print proceeds

Since the final grain is too big for the printer enclosure and problems with the part sticking to the bed could arise, it was decided to divide the print in 4 parts that would then be glued together (each part takes around 18 hours to be printed).

To assess the quality and properties of the printed product a simple cylindrical grain (same as the one used for baseline data) was first printed and then the burned sample compared with a traditionally manufactured grain (see section 5.3.2). This was done specifically to determine if the 3D printed grain can be compared with a traditionally machined grain; if the difference is consistent, all fuel grains - both baseline and helical - will need to be 3D printed.

During the print tests it was key that the process could be remotely monitored (Fig. 5.14); this was made possible thanks to the *BambuLab Slicer* app for desktop or mobile. It was especially helpful to tailor bed and chamber temperatures as the print progressed.

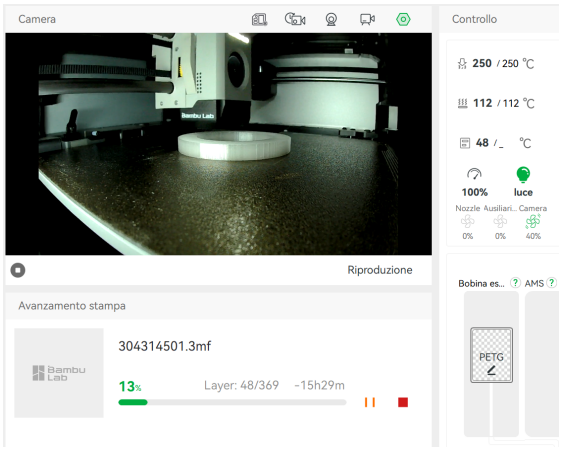

Figure 5.14: Screen Shot of a print being remotely monitored

5.3.2 Traditionally Machined Grains

During the test campaign, traditionally machined PMMA grains were also used. Each grain is composed by two halves, individually manufactured in order to ease the process.
The manufacturing process starts from a 4 ft acrylic rod, that needs to be cut into pieces approximately of the same length of the half grains (they will be machined to the exact length later). This procedure was done on a horizontal bandsaw in the students shop (Mustang 60 Machine Shop) or in the M.E. Department technical shop.
All the following steps of the process are done on a CNC lathe. The halves are subsequently:

- Faced, so that they are the correct length (half the chamber) with cuts as perpendicular as possible.
- Drilled, with an appropriate tail stock in order to have a starting hole that will then be extruded so that the ID is the desired size.
- Turned, for both the ID and OD to the desired values.

At the time that this project was carried, some already machined grains were available at the engines lab; only the last step (Fig. 5.15) was needed to make the cylinder grains fit into the phenolic liners (cylinders used as thermal insulators to avoid overheating the stainless steel chamber).

The two parts that form the grain are glued together using a special high temperature resistant silicone (RTV) and then inserted in the phenolic liner. If the

Figure 5.15: Half grain on a CNC Lathe before its OD is turned

grain and the liner were not able to hold a press-fit, RTV silicone was used to glue the two parts, in order to prevent the grain from moving when the rocket was fired (Fig. 5.16).
To insert the grain-liner assembly into the chamber, the bore press at the M.E. Department technical shop was used (Fig. 5.17); the same machine was also used to extract the burned grain from the chamber when it had to be measured.

Figure 5.16: Grain inserted in a liner next to the combustion chamber

Figure 5.17: Grain-Liner assembly being press fit into the combustion chamber

5.3.3 Phenolic Liner Machining

As briefly mentioned above, the PMMA fuel grains are fit into phenolic liners before being inserted into the combustion chamber.
The liners serve as thermal protection to avoid overheating the stainless steel combustion chamber.

A phenolic tube would need to be cut into pieces as long as the chamber using a meter saw or horizontal bandsaw and then turned on a lathe to fine tune the OD so it would press fit into the chamber.

Unfortunately, since phenolic dust can be toxic, it was not possible to machine new phenolic liners for this project. It was then decided to re-use some of the liners used during past firing tests.

Chapter 6

Test Campaign

The first actual test of the rocket motor was carried out to asses the ability to start the system using the ignition gasses (Fig. 4.5) propane and oxygen; for this test an old PMMA grain that was already burned was used and the nozzle wasn't installed, as the sole objective of the test was to successfully ignite the engine.
After this test was deemed successful, a proper test with an unused PMMA simple cylinder grain was carried out in order to obtain baseline data.

6.1 Data Acquisition and Methodologies

This section focuses on how data was acquired during the test campaign and how it was used to calculate performance parameters such as the regression rate.

6.1.1 Sensor Data Acquisition

As already discussed, sensors ere used to acquire temperature and pressure data through a *LabVIEW* interface. Data from 5 thermocouples and 2 pressure transducers was simultaneously acquired at around 20 Hz data sampling rate and was then saved in a dedicated excel file.

The pressure data was then also used to determine the burn time of each test by tracking the changes in pressure. The engine was considered to be "ON" when the pressure reached around 15% of the steady state pre-chamber pressure, and was considered "OFF" when, once the N_2O was stopped from flowing, the pressure reached again 15% of the steady state.

6.1.2 After-burn Measurements

After each test, the grains were extracted from the chamber to be measured. The dimension measured was the internal diameter (ID). The measurement procedure followed was:

- The grain was marked every 1.5 cm along the axis using calipers and a sharpie or pencil. The marks serve as a guiding line to know where to take measurements of ID.
- Bore gauges were inserted in the grain to the desired depth and then locked to get a ID measure.
- The bore gauge was then measured using calipers and the ID value (in mm) was reported in an excel file.

For each axial position, the ID was measured at least 2 times, to account for possible non-uniformity in the radial plane.

These measurements were then used to calculate the local regression rate values, as:

$$\dot{r}^i_{loc} = \frac{(D_i)/2}{t_{burn}} \tag{6.1}$$

where i is the indicator for the data relative to the i-th axial location.
The average regression rate was calculated as:

$$\dot{r}_{avg} = \frac{(\sum_i (D_i/2))/n}{t_{burn}} \tag{6.2}$$

where n is the number of axial location considered for the measurements.

6.2 Hotfire Tests Results

6.2.1 Summary of Configurations Tested

It's important to report the various possible configurations for the injection plate and the propellant grain, as the tight schedule forced the choice of the configurations to be tested.

The injection plate configurations considered were:

- Axial configuration: six axial injectors were screwed in place; the six remaining injection holes were capped with bolts.
- Swirl configuration: six swirl injectors are used and the other holes are capped with bolts.
- Mixed configuration: three swirl injectors and three axial injectors are used.

Concerning the propellant grains, three possible grains are considered for the test campaign:

- Traditionally machined simple cylinder grain, from here on called traditionally machined baseline.
- Additively manufactured simple cylinder grain, from here on called 3D Printed baseline.
- Additively manufactured grain with helical guide vanes, from here on called 3D Printed helical grain.

Table 6.1 reports the test matrix for this project. Each configuration was tested once, as the schedule for the project was tight after the lab revamping process. Only the most important or interesting configurations were tested.

	Axial Injection	Swirl Injection	Mixed Injection
Trad. Machined Baseline	x	x	
3D Printed Baseline	x		
3D Printed Helical Grain			x

Table 6.1: Test Matrix. The combinations tested are marked with an "x"

6.2.2 Baseline Grain

The rocket was first fired on October 31st; unfortunately, the N2O was flowed in the chamber for too long, causing the complete comsumption of the PMMA grain and the start of the ablation of the phenolic liner.
The test was deemed successful either way, as the rocket was lit and the N2O did not extinguish the flame. In Fig. 6.1 a frame of the engine that is being fired is shown.

Figure 6.1: First Hot Test carried at Cal Poly after the refurbishment of the test cell

To make up for the data that was not possible to acquire (internal radius at different axial locations for regression rate calculations), a hot test previously conducted at Cal Poly was used [26]. Table 6.2 summarizes the test characteristics.

Parameter	Value	Unit
Burn Time	14	s
Burned Grain	450	g
N2O Burned	2.5	kg

Table 6.2: Test Characteristics

The burned PMMA grain was then measured at different axial locations. In Fig. 6.2 the measurements are compared with the internal radius predicted by Marxman's model

$$\dot{r}_{loc} = aG^n x^m \tag{6.3}$$

The predicted values are in accordance with the measurements, with a clear

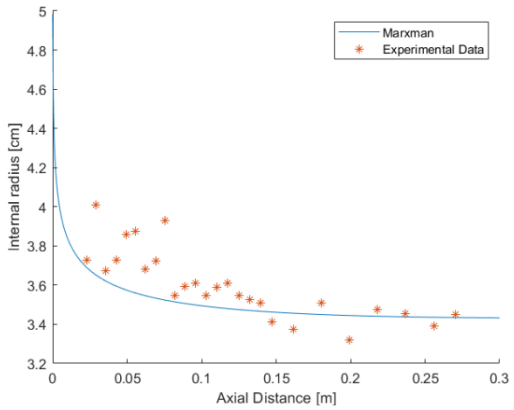

Figure 6.2: Measured data and predicted values from Marxman's model integration

difference in the final radius between the injection end and the nozzle end of the grain, due to the entrance effects caused by the axial injectors.
For ease of visualization, the grain geometry after the burn was plotted, so that the difference in internal diameter could be assessed (Fig. 6.3).

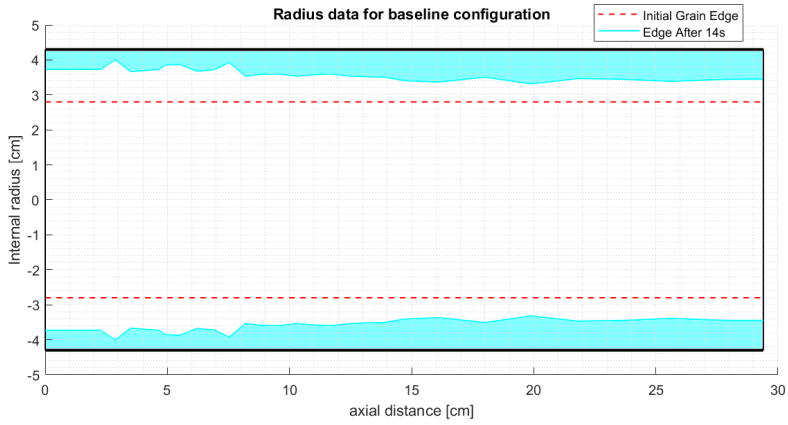

Figure 6.3: Internal diameter after 14 s of burn time for the baseline grain

It's possible to see the great dis-uniformity in the internal diameter and hence in the local regression rate. The local regression rate was then calculated using the measured data and the time of burn, obtaining what is shown Fig. 6.4.
The average regression rate was computed to be:

$$\dot{r} = 0.567 \ mm/s \tag{6.4}$$

For the purpose of this project, it's important to analyze the uniformity level in the local regression rate along the length of the grain.

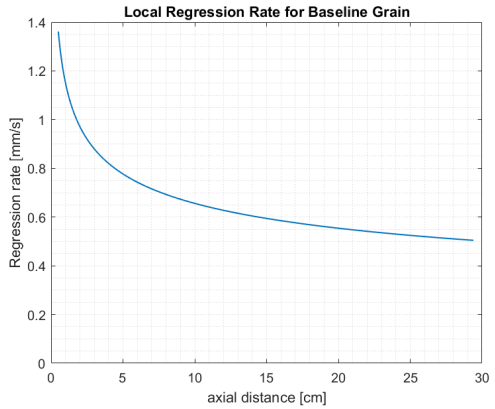

Figure 6.4: Regression rate trend with the axial position along the grain

To to so, the maximum and minimum local regression rate (obtained at the injection and nozzle end respectively) are compared between each other (from here on called Uniformity Test 1); as another way to asses the dis-uniformity of the burn, the local regression rate at different axial locations is also compared to the average regression rate and to the maximum local regression rate (from here on Uniformity Test 2). For these comparisons and the following ones, all percent values reported are calculated as ratios, such as: $\% = \frac{Value_i}{Comp.Value} * 100$.

The results of this comparison are shown in Table 6.3; there is an important difference between the maximum and minimum local regression rate, with the second one being less the half the first. Besides, injection and nozzle end in both the comparisons reported are very different and the regression rate is overall not uniform, leaving a considerable room for improvement. The table also explains what is shown in Fig. 6.3.

Uniformity Test 1				
Max $\dot{r}$ $[mm/s]$	0.864	Min to Max Ratio (%)		
Min $\dot{r}$ $[mm/s]$	0.371	42.9%		
Uniformity Test 2				
Axial Location	at 3 cm	at 12 cm	at 18 cm	at 28 cm
% of avg. $\dot{r}$	152.4	98.23	89.41	81.86
% of max $\dot{r}$	100	64.46	58.68	53.72

Table 6.3: Uniformity Level in the baseline regression rate

6.2.3 3D Printed Baseline Grain

In order to assess possible differences in performance by switching to a different grain manufacturing technique (going from "store-bought" machined PMMA to additive manufacturing), a 3D printed simple cylindrical grain was fired with the purpose of later comparing the results with the "traditional" grain (Section 6.2.1). Table 6.4 shows the test characteristics. The test was purposefully run for a short period of time as a safety precaution since the quality of the burn was unknown.

Parameter	Value	Unit
Burn Time	10.8	s
Burned Grain	380	g
N2O Burned	1.8	kg

Table 6.4: Test Characteristics

After the test, the grain internal diameter was measured using bore gauges and calipers at different axial locations. The reconstruction of the grain edge is shown in Fig. 6.5. It can be seen that this grain also shows a great level of dis-uniformity in the internal diameter.

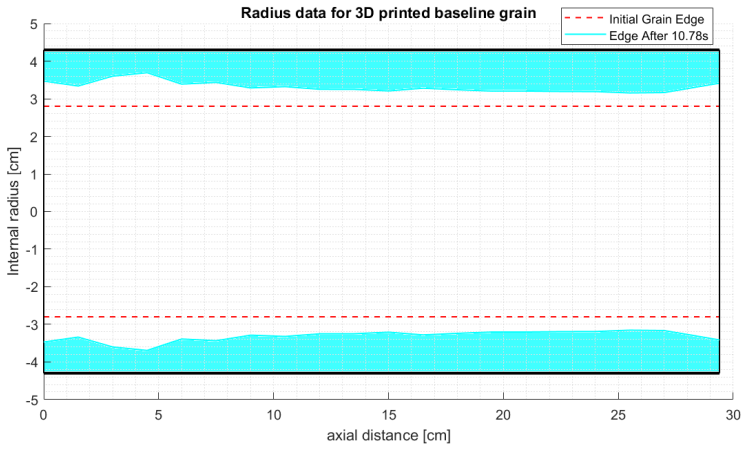

Figure 6.5: Internal Diameter after 10.78s

The average regression rate was calculated to be:

$$\dot{r} = 0.437 \; mm/s \tag{6.5}$$

The local regression rate values were calculated using the same process employed for the previous test; the results are shown in Fig. 6.6. As it can be seen the test

shows a clearly decreasing trend in the regression rate when going towards the nozzle end of the motor.

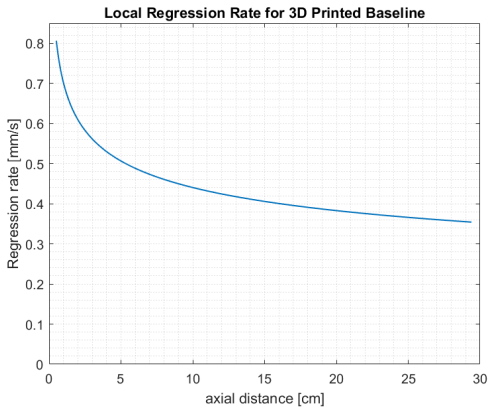

Figure 6.6: Local regression rate trend for 3D printed simple cylinder grain

For this grain too the level of uniformity in the regression rate was analyzed. The results of the analysis are reported in Table 6.5. This test, like the previous one, shows a considerate dis-uniformity in the regression rate along the length of the grain, with the nozzle end regression rate being 70.95% of the maximum regression rate (measured at 4.5 cm from the start of the grain). This demonstrates that the injection effects are independent from the manufacturing technique of the grain.

Uniformity Test 1				
Max $\dot{r}$ $[mm/s]$	0.758	Min to Max Ratio (%)		
Min $\dot{r}$ $[mm/s]$	0.301	39.7%		
Uniformity Test 2				
Axial Location	at 3 cm	at 12 cm	at 18 cm	at 27 cm
% of avg. $\dot{r}$	173.5	87.81	85.37	70.95
% of max $\dot{r}$	89.67	50.61	49.21	40.89

Table 6.5: Uniformity Level in the baseline regression rate

6.2.4 Swirl Injection Test

The helical guide vanes in the novel geometry serve the purpose of maintaining the swirl motion imparted by the swirl injectors previously manufactured at Cal Poly (Fig. 6.7 [14]). It's understandable that knowing the axial location at which the swirl "naturally" decays inside the cylinder grain is key for the correct design of the vanes as it will determine where they will start. To do so, a simple traditionally

machined PMMA grain was fired using 6 swirl injectiors and its ID was then measured along the length to identify the axial position where the swirl decays (a difference in the regression rate is visible for the part that benefits from this type of injection).

Figure 6.7: Swirl injector before being mounted into the pre chamber

The 6 injectors were mounted as specified by the colleague that manufactured them in order to obtain the swirl number that they were designed for.
The engine was fired for approximately 12 seconds. Thanks to the measurements, it was possible to reconstruct the internal shape of the grain and assess the swirl effects (Fig. 6.8).

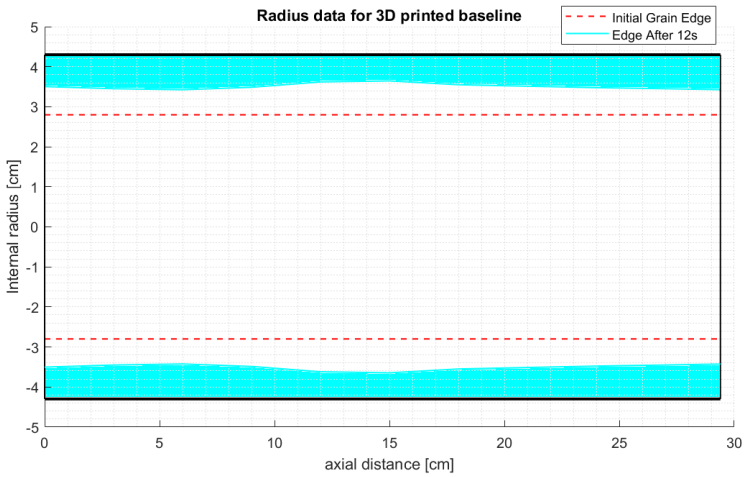

Figure 6.8: Reconstructed grain with swirl injection scheme

As seen, the grain shows an increased regression rate in a section about 7 cm long starting at around 9 or 10 cm from the injection end (with a maximum at around 13 cm). This goes to demonstrate that the injectors work as they were machined to: the goal of the previous colleague's thesis was indeed to create a swirl injection

system that would impinge around 10 cm into the grain [14], without generating a recirculation zone at the entrance that would create what is seen in Figs. 6.3 and 6.5. A drawback of having a swirl number as low as the one adopted in this configuration is the fact that the swirling motion quickly decays as the tangential momentum is not strong enough to carry on to the end of the fuel grain; this is visible both from the reconstruction in Fig. 6.8 and in Table 6.6 were the regression rate at different axial locations is presented.

Axial Location	at 6 cm	at 15 cm	at 24 cm	Nozzle End
% of average $\dot{r}$	88.78	120.1	96.09	88.92
% of max $\dot{r}$	73.95	100.0	80.03	74.07

Table 6.6: Comparison of regression rate at different locations

The average regression rate was calculated to be:

$$\dot{r} = 0.538 \ mm/s \tag{6.6}$$

6.2.5 3D Printed Helical Grain

After analyzing the results present in section 6.1.3, it was decided to test the helical geometry using 3 swirl injectors and 3 axial injectors combined together (Fig. 6.9) in an attempt to boost the regression rate along the whole grain; ideally, this configuration, would still present a good regression rate at the injection-end (but lower compared to the one obtained with only axial injectors) while in the second and last thirds of the grain the swirl motion imparted by the injectors and the geometry would take over in the enhancement process, ensuring a sort of balance in the regression rate along the grain.

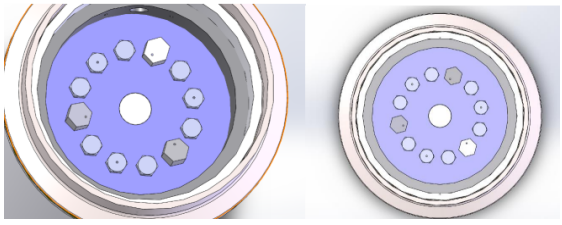

Figure 6.9: Mixed axial-swirl injection configuration

The test characteristics are reported in Table 6.7.
Fig. 6.10 shows a before and after comparison of the grain.
After the test was completed, the grain was removed from the chamber and measured

Parameter	Value	Unit
Burn Time	11.7	s
Burned Grain	460	g
N2O Burned	1.7	kg

Table 6.7: Test Characteristics

Figure 6.10: Visual comparison of the helical grain geometry before and after the hot test

using bore gauges and calipers at different axial location in order to obtain the local internal diameter after the burn. The reconstruction of the grain edge was obtained as for the other tests and is displayed in Fig. 6.11.

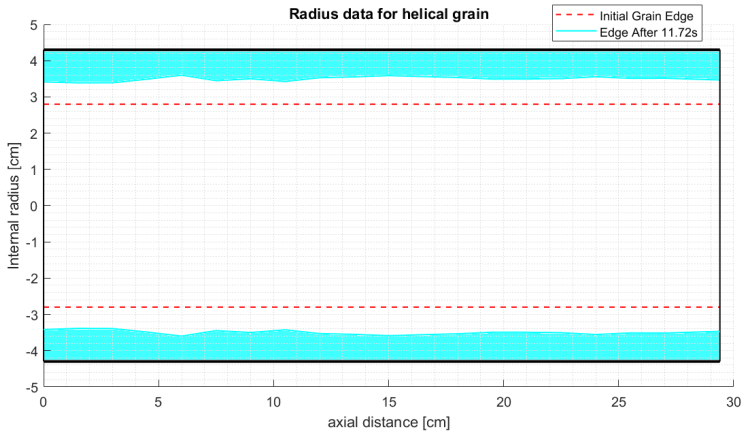

Figure 6.11: Reconstruction of the rain edge of the Helical Grain after the hot test

The average regression rate was calculated to be:

$$\dot{r} = 0.597 \ mm/s \tag{6.7}$$

One of the key goals for this project is to obtain a higher level of uniformity in regression rate, so the uniformity tests have been conducted for this new geometry, obtaining Table 6.8.

Uniformity Test 1				
Max $\dot{r}$ $[mm/s]$	0.682	Min to Max Ratio (%)		
Min $\dot{r}$ $[mm/s]$	0.501	73.5%		
Uniformity Test 2				
Axial Location	at 3 cm	at 12 cm	at 18 cm	at 27 cm
% of avg. $\dot{r}$	84.64	104.5	105.3	102.4
% of max $\dot{r}$	73.93	91.31	92.00	89.44

Table 6.8: Uniformity Level in the helical grain regression rate

As it can be seen from the results of Uniformity Test 1, the geometry exhibits a great level of uniformity: the minimum regression rate (measured at 1.5 cm) is almost 3/4 of the maximum regression rate (measured at 6 cm). The grain shows a lower regression rate at the injection end, and it doesn't present the classic injection effects that were seen in previous tests due to the recirculation zone generated by the 3 axial injection being weakened by the 3 swirl injectors.
Uniformity Test 2 shows that the geometry is able to produce a good level of regression rate uniformity along the grain length. This goes to demonstrate that the helical guide vanes designed helped carry the swirling motion forward and didn't let it decay as fast as it's seen in section 6.1.3.
The level of uniformity can also be visually seen by plotting the measured regression rate values along the axis (Fig. 6.12). The average regression rate is added for context.

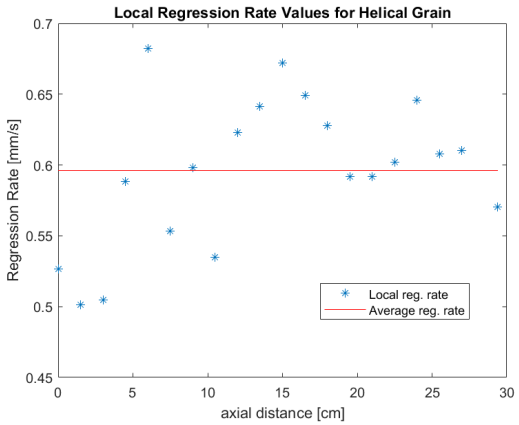

Figure 6.12: Regression rate values for the helical grain

6.3 Comparison Between Tests

In this section, different test configurations are compared to each other. The first comparison (Section 6.3.1) compares the two "baseline" tests, the traditionally machined PMMA grain and the 3D printed cylinder, respectively, with the aim of assessing the difference in performance of the two manufacturing techniques. This first comparison also serves to choose which of the two configurations will be used to assess the enhancement obtained with the helical grain configuration.
The second comparison (Section 6.3.2) serves to study the enhancements carried out by the proposed geometry of this project.

6.3.1 3D Printed vs Traditionally Machined Baseline Grains: axial injection

As anticipated, this section compares the two "baseline" tests as they need to be compared to assess possible differences in the performance of the motor. As seen in Table 6.9, the two tests were performed under the same conditions and with the same type of injectors. The only difference is in the burn time, a parameter that could not be automated and was difficult to control precisely, so the 3D printed burned for 10.78 s and the traditional one for 14 s.

Parameter	Traditional	Additive Manufacturing
Burn Time [s]	14	10.78
Injection Scheme	6 axial inj.	6 axial inj.
Grain Length [cm]	29.4	29.4
Grain ID [cm]	5.8	5.8
Grain OD [cm]	8.6	8.6

Table 6.9: Test Characteristics comparison

To account for the difference in burn time it was decided to simulate the burn of the 3D printed grain for the Δt remaining to get to a 14s burn; this was done using a custom made *MATLAB* script that calculates the internal radius of the grain at different axial location with a $dt = 0.2s$.

The first comparison carried was a visual inspection of the two burned grains (Fig. 6.13). The samples exhibit very different after-burn conditions, with the additively manufactured grain having a "coarser" surface when compared to the smoother traditionally manufactured grain. Both grains show a level of charring (the 3D printed went from being white to black, while the traditional grain went from being almost transparent to dark grey).

Figure 6.13: Visual comparison of the two baseline grains. On the left the 3D printed grain, on the right the traditionally machined

The difference in surface finish is to be attributed to the different manufacturing technique. The roughness of the internal surface of the 3D printed grain is probably due to the fact that the flow rate flows perpendicular to the filament "layers" that make up the grain and to possible microscopic air pockets left during the printing process. The combustion process then uncovers the interface between the various layers causing the roughness observed. In order to actually understand the cause of this difference and how to effectively tackle it, more tests should be performed, which unfortunately was not possible due to time constraints.

The second comparison regards the results obtained by the two configurations. Table 6.10 and Fig. 6.14 compare the average and local regression rates respectively. The 3D printed grain shows a considerably lower regression rate compared to the traditional grain, being only 77%; this difference is probably to be attributed to the different ways the two grain burn, but more tests are needed to confirm.

The trends in the regression rates follow the same behavior, with a higher regression rate at the injection end, followed by a sharp decline and then the decrease rate becomes milder going towards the nozzle end. This goes to show that the injection effect doesn't depend on the grain manufacturing technique, but it's a phenomenon only dependent on the injection scheme adopted.

Traditional Grain	3D Printed Grain	Ratio
0.567 mm/s	0.437 mm/s	77%

Table 6.10: Average regression rate comparison

Even though the local regression rate trend is similar between the two grains (with the ratios between max and min being 40% and 43% for 3D printed and traditional respectively), the considerable difference in the average regression rate (and hence

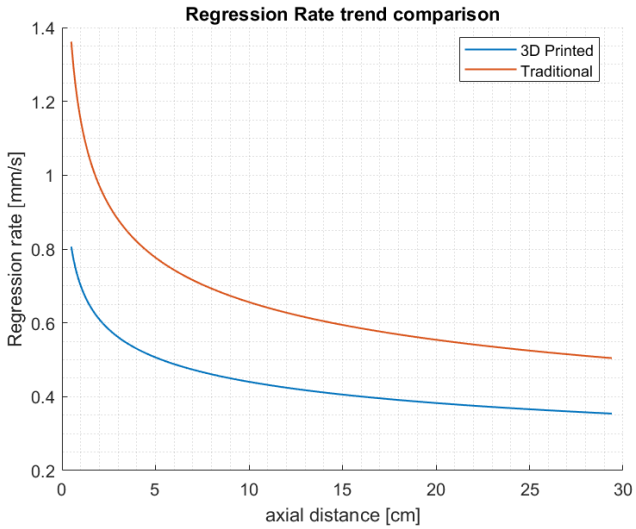

Figure 6.14: Comparison of local regression rate trend

in the local regression rate values - Fig. 6.15 highlights the difference in the internal diameter measured) and the difference observed in the visual comparison led to deem the two manufacturing techniques not comparable.

The 3D printed baseline test was chosen as the one to be compared with the proposed geometry, as they were both obtained via additive manufacturing.

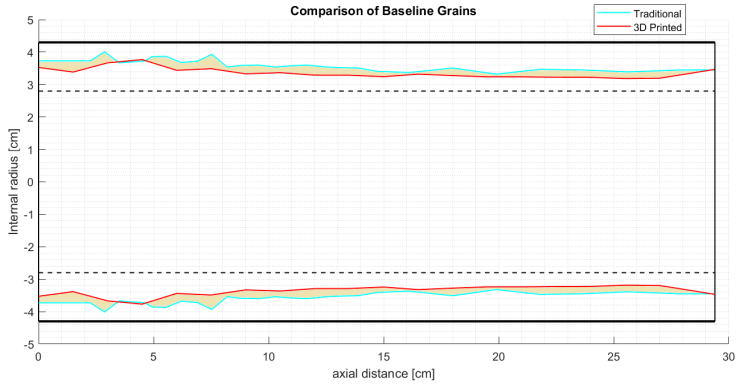

Figure 6.15: Grain edge comparison between the two baseline configuration. The edge for the 3D grain was obtained by simulating the burn to match the same burn time of the traditional grain

6.3.2 Helical Grain (mixed injection) vs 3D Printed Baseline (axial injection)

This comparison aims to understand the level of enhancement that the helical vanes can bring to the regression rate both on the average value and on the local one. The tests were conducted for a similar amount of time as burn time is 10.78 s and 11.83 s for baseline and helical respectively. Table 6.11 shows the comparison between the two tests.

Parameter	3D Printed Baseline	Helical Grain
Burn Time [s]	10.78	11.83
Injection Scheme	6 axial inj.	3 axial and 3 swirl inj.
Grain Length [cm]	29.4	29.4
Grain ID [cm]	5.8	6.0 (avg)
Grain OD [cm]	8.6	8.6

Table 6.11: Test Characteristics comparison

To account for the different burn time (although the difference is not as big as for the previous comparison), the 3D printed baseline grain burn was simulated until the burn times matched.

The first comparison carried is between the reconstructions of the two grains' edges after the burn (Fig. 6.16). The helical grain shows a higher internal diameter (hence a higher regression rate) and a more uniform burn along the axis when compared to the simple 3D printer cylinder grain. This means that the thesis goals of better performance (average regression rate) and better uniformity of the local regression rate along the length of the grain, are met at least at a qualitative level; in order to assess the level of improvement brought by the new geometry and injection scheme pairing, more comparisons are presented in the following pages.
A quantitative comparison is to be made to assess the enhancement in the average regression rate brought by the helical guide vanes (Table 6.12). The helical grain shows a considerably higher average regression rate, with a 36.4% enhancement compared to the 3D printed simple cylinder grain.
From Fig. 6.16 it's possible to make assumptions about the regression rate: the baseline grain has a slightly better regression rate at the injection end of the motor, given by the injection effects of having 6 axial injectors, while the helical grain has a lower value because the configuration only uses 3 axial injectors. At 6 cm from the start of the cylinder, the helical grain starts to have a better regression rate, thanks to the swirl jets starting to impinge on the grain surface and then the helical guide vanes beginning at 12 cm.
It's also interesting to compare the maximum and minimum values of the regression

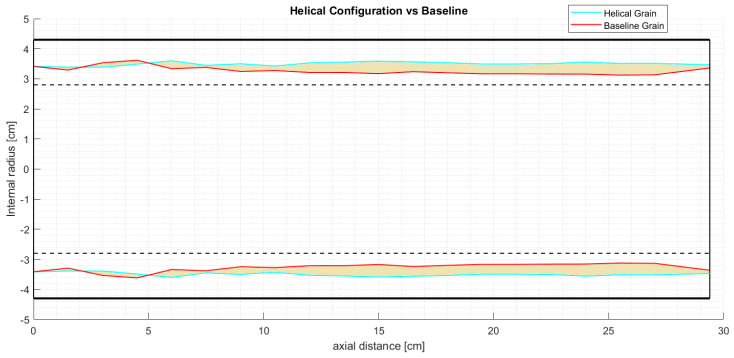

Figure 6.16: Comparison of grain edges. The difference is highlighted in yellow

3D Printed Baseline	Helical Grain	% Enhancement
0.437 mm/s	0.596 mm/s	36.4%

Table 6.12: Average regression rate comparison

rate that the two configuration exhibit (Table 6.13). The 3D printed baseline grain shows a higher maximum regression rate (11% higher), measured close to the injection-end of the grain. The helical grain has a considerably higher minimum in regression rate (66% higher) when compared to the 3D baseline.

	3D Printed Baseline	Helical Grain
Maximum $\dot{r}$ [mm/s]	0.758	0.682
Minimum $\dot{r}$ [mm/s]	0.301	0.501
Location of max [cm]	4.5	6.0
Location of min [cm]	25.5	1.5

Table 6.13: Comparison of maximum and minimum regression rate values

It is interesting to note that the minimum for the two configurations are measured at the opposite ends of the propellant grains: while the 3D baseline grain shows the lowest regression rate at the nozzle-end of the motor (in accordance with the theoretical prediction and the experimental evidence in literature), the helical configuration has its minimum at the injection-end of the motor (measured at 1.5 cm); this is evidence of the fact that the proposed configuration considerably reduces the injection effects that were seen in both baseline configurations.

Another goal of this thesis is to obtain a more uniform local regression rate along the length of the propellant grain. To assess if the objective is successfully achieved the local regression rates measured are first visually compared in Fig.

6.17. It can be seen that the helical configuration shows a definitely better level of uniformity when compared to the 3D printed baseline grain. The percent offset from the average regression rate can be measured as follows:

$$\% \; Offset = \frac{\dot{r}_{loc} - \dot{r}_{avg}}{\dot{r}_{avg}} * 100 \tag{6.8}$$

By comparing the average percent offset of the two configurations it's possible to understand the enhancement brought by the helical grain.
The helical grain has an average offset from its average regression rate of 6.75%, against the 3D printed baseline's 22.3%. Hence, the guide vanes are a good solution to increase the regression rate in the second half of the grain.

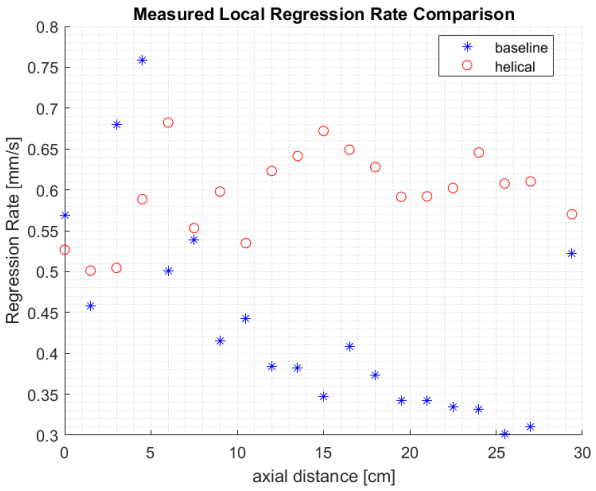

Figure 6.17: Comparison of the measured local regression rate values for the two configuration

Table 6.14 summarizes the comparison of the regression rate measurements for the uniformity enhancement assessment. As already discussed before, the helical grain shows a better average offset from the average regression rate, but it's also important to note that the maximum offset is also considerably lower when compared to the additively manufactured baseline grain (it can also be seen in the measurements distribution in Fig. 6.17).

Another interesting comparison that can be made is about the chamber pressure for the two tests, as it gives an idea of the thrust the geometry is able to create. Unfortunately, even though a load cell was present in Cal Poly's hybrid rocket stand, it was not possible to use it due to the instrument not being calibrated. To have an idea of the level of thrust produced it was then decided to use the pressure

	3D Printed Baseline	Helical Grain
Avg. Offset from $\dot{r}_{avg}$ [%]	22.3	6.75
Maximum Offset from $\dot{r}_{avg}$ [%]	73.5	14.5
Min/Max $\dot{r}$ ratio [%]	39.7	73.5

Table 6.14: Uniformity Level comparison between 3D printed baseline and helical grain

measured by the pressure transducer in the pre-chamber.
Fig. 6.18 shows the pressure in *psig* for the two different configurations. The pressure for the 3D printed baseline is at around 188 psig, in line with the pressure measured during the traditionally machined baseline test and previous tests carried at Cal Poly in the past. The helical grain exhibits a higher pressure, around 218 psig.

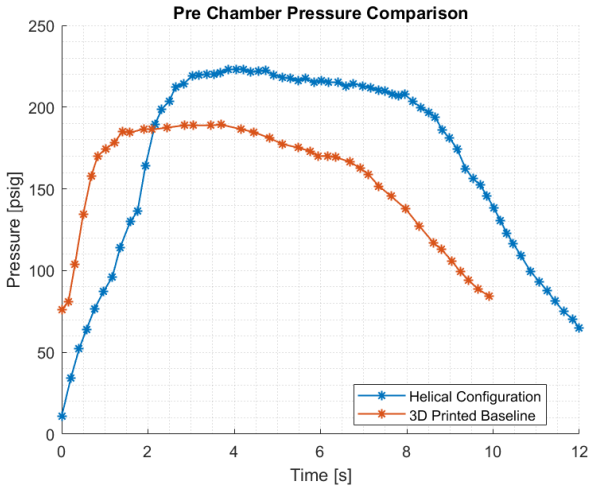

Figure 6.18: Comparison of the pressure produced in the pre chamber by the two different geometries

A higher pressure leads to higher trust produced by the rocket, using the equation

$$F = \dot{m}V_e + (p_e - p_0)A_e \longrightarrow F = C_F p_c A_t \tag{6.9}$$

Since the nozzle and the ambient conditions are the same for the two tests conducted, it can be concluded that the geometry proposed in this study is also able to produce a higher thrust compared to a simple cylindrical grain. This is alos due to the fact that the helical grain has a higher internal burning surface thanks to the guide vanes (591.2 cm^2 against the 535.4 cm^2 of the baseline - 10% higher); this leads to a more favorable mass flux and hence a higher thrust.

Chapter 7

Conclusions and Future Work

7.1 Conclusions

This project proposed an injection scheme and grain geometry configuration with the aim of increasing the average regression rate produced by the PMMA-N2O combination while also obtaining a more uniform local regression rate.
The configuration proposed consists of the combination of a swirl injection system, previously machined at Cal Poly, and helix guide vanes in the internal surface of the grain that match the swirl created by the injectors to bring it to the nozzle end.

After analyzing the results of the test campaign, an increase in the average regression rate of 36% was measured, so the first goal was successfully met. This was obtained thanks to a higher level of turbulence brought by the swirl motion, leading to an increase in the heat exchange between the grain surface and the combustion gasses.

The objective of a more uniform local regression rate was also met, as the helical configuration shows a percent offset from its average regression rate of 6.75%, greatly increasing the uniformity level from the baseline grain's 22.3% offset. It was also found that the min to max ratio of the regression rate is more favorable, with the minimum regression rate being 73.5% of the maximum against the baseline's 39.7%.

A secondary result of this thesis project is the fact that it was deemed not possible to compare a 3D printed grain with one traditionally machined on a lathe. Their performances, especially regarding the average regression rate, are not comparable,

with the additively manufactured grain having a considerably lower regression rate.

Unfortunately, due to scheduling reasons and the lab refurbishment taking a lot longer than expected, it wasn't possible to conduct extensive testing of the hybrid rocket motor. This has to be accounted for future work.

7.2 Future Work

In future work it has to be considered key to conduct more tests with what has been proposed in this work, in order to assess the repeatability of the experiments and other performance parameters such as thrust for example.
Other than this, various interesting paths could be studied to add to this field of research.

The first one being an optimization of the parameters of the configuration, such as swirl number (that can be modified by machining new injectors), injection scheme (by changing the number of axial and swirl injectors) and parameters of the internal geometry (helix pitch and grooves characteristics) with the aim of finding a maximum enhancement in performances.

Another interesting addition is a study aiming to understand what causes the differences in performance observed when comparing 3D printed grains and traditionally machined grains. Extensive testing could help understand possible differences in ballistic coefficients and in the critical velocity for the charring effect observed in the burnt samples.

Bibliography

[1] G. P. Sutton and O. Biblarz. *Rocket Propulsion Elements*. Ninth Edition. Wiley, 2017 (cit. on pp. 1, 3, 6, 7, 9).

[2] D. Pastrone. «Approaches to Low Fuel Regression Rate in Hybrid Rocket Engines». In: *International Journal of Aerospace Engineering* (2012) (cit. on pp. 2, 9, 10, 13, 14).

[3] D. Kaniewski A. Okninski W. Kopacz and K. Sobczak. «Hybrid rocket propulsion technology for space transportation revisited propellant solutions and challenges». In: *FirePhysChem* 1 (Dec. 2021), pp. 260–271 (cit. on pp. 3, 4).

[4] E. T. Jens. «Hybrid Rocket Combustion and Applications to Space Exploration Missions». PhD thesis. Stanford University, 2015 (cit. on p. 6).

[5] G. A. Marxman and M. Gilbert. «Turbulent Boundary Layer Combustion in the Hybrid Rocket». In: *Symposium (International) on Combustion* 9 (1963), pp. 371–383 (cit. on p. 6).

[6] R. Muzzy G. A. Marxman and C. Wooldridge. «Fundamentals of hybrid boundary layer combustion». In: *American Institute of Aeronautics and Astronautics* (1963) (cit. on pp. 6, 8).

[7] C. Carmicino and A. Russo Sorge. «Influence of a Conical Axial Injector on Hybrid Rocket Performance». In: *Journal of Propulsion and Power* 22 (2006), pp. 984–995 (cit. on p. 10).

[8] J. M. Beer A. K. Gupta and N. Syred. *Swirl flows*. Abacus Press, 1984 (cit. on pp. 11, 13).

[9] H. Hachiya S. Yuasa K. Yamamoto and K. Kitagawa. «Development of a small sounding hybrid rocket with a swirling-oxidizer-type engine». In: *Proceedings of the 37th Joint Propulsion Conference* (2001) (cit. on p. 14).

[10] S. Aso K. Ozawa K. Kitagawa and T. Shimada. «Hybrid Rocket Firing Experiments at Various Axial–Tangential Oxidizer-Flow-Rate Ratios». In: *Journal of Propulsion and Power* 35 (2019), pp. 94–108 (cit. on p. 14).

[11] Y. Na C. Lee and G. Lee. «The Enhancement of Regression Rate of Hybrid Rocket Fuel by Helical Grain Configuration and Swirl Flow». In: *41st AIAA/ASME/SAE/ASEE Joint Propulsion Conference Exhibit* (2005) (cit. on pp. 15, 33, 38, 42, 45).

[12] J. Zhu X. Wang W. Yuchi and J. Yao. «Heat Transfer Enhancement and Vortex Flow Structure in the Spirally Fluted Tubes». In: *Journal of Thermal Science* 30 (2021), pp. 1814–1826 (cit. on pp. 15, 16).

[13] P. Promthaisong et alles. «Numerical investigation on turbulent forced convection and heat transfer characteristic in spirally semicircle-grooved tube». In: *International Journal of Mechanical and Materials Engineering* (2016) (cit. on p. 16).

[14] G. Quartararo. «Design and Test of a Swirling Nitrous Oxide Injection System for a Hybrid Rocket Motor». Aero. Eng. Thesis. Turin, Italy: Politecnico di Torino, July 2020 (cit. on pp. 19, 43, 45, 46, 59, 61).

[15] *Data Acquisition Basics Manual*. National Instruments. 1998 (cit. on p. 22).

[16] *Modbus Master Library User Guide*. Plasmionique Inc. 2019 (cit. on p. 22).

[17] *Micro Motion Modbus Interface Tool Integer Scaling*. Emerson Process Management. 2008 (cit. on p. 23).

[18] National Instruments. *LabVIEW Tutorial*. URL: `https://learn.ni.com/learn/article/labview-tutorial` (cit. on p. 23).

[19] Valydine Engineering YouTube Channel. *Changing a Diaphragm in a Validyne Pressure Sensor*. URL: `https://www.youtube.com/watch?v=e9duxWfDzkE&t=75s&ab_channel=ValidyneEngineering` (cit. on p. 26).

[20] C. Li H. Tian Y. Li and X. Sun. «Regression rate characteristics of hybrid rocket motor with helical grain». In: *Aerospace Science and Technology* 68 (2017), pp. 90–103 (cit. on pp. 33, 37, 40, 41, 44).

[21] Y. Na C. Lee and Y.C. Hwang. «Turbulent flow in the helical grain of hybrid rocket fuel». In: *42nd AIAA/ASME/SAE/ASEE Joint Propulsion Conference Exhibit* (2006) (cit. on pp. 33, 37–39).

[22] Y. Byun C. Lee J. Lee. «Effect Of Induced Swirl Flow On Regression Rate Of Hybrid Rocket Fuel By Helical Grain Configuration». In: *European Conference For Aerospace Sciences (EUCASS)* () (cit. on pp. 33, 37, 38, 40, 42, 43, 45).

[23] S. Young Chang K. H. Shin C. Lee. «The Enhancement of Regression Rate of Hybrid Rocket Fuel by Various Methods». In: *43rd AIAA Aerospace Sciences Meeting and Exhibit* (2005) (cit. on pp. 33, 37, 38, 40).

[24] H. Gul K. Bilen M. Cetin and T. Balta. «The investigation of groove geometry effect on heat transfer for internally grooved tubes». In: *Applied Thermal Engineering* 29 (2009), pp. 753–761 (cit. on pp. 33, 35, 40).

[25] E. T. Idowu T. S. Mogaji A. O. Olapojoye and B. Saleh. «CFD study of heat transfer augmentation and fluid flow characteristics of turbulent flow inside helically grooved tubes». In: *Journal of the Brazilian Society of Mechanical Sciences and Engineering* (2022), pp. 44–90 (cit. on pp. 33, 37, 40).

[26] G. Cipolla. «Grain Geometry Effects on a Hybrid Rocket Engine Performance». Aero. Eng. Thesis. Turin, Italy: Politecnico di Torino, July 2020 (cit. on pp. 45, 55).